https://doi.org/10.5194/egusphere-2025-5665
Preprint. Discussion started: 19 November 2025

Secondary ice production affects tropical convective clouds under different aerosol conditions

Mengyu Sun[1], Paul J. Connolly[1], Paul R. Field[2,3], Declan L. Finney[3,4], Alan M. Blyth[4,3]

[1] Department of Earth and Environmental Sciences, University of Manchester, Manchester, UK
[2] Met Office, Exeter, UK
[3] Institute for Climate and Atmospheric Science, School of Earth and Environment, University of Leeds, Leeds, UK
[4] National Centre for Atmospheric Science, Leeds, UK

Correspondence to: Mengyu Sun (mengyu.sun@manchester.ac.uk)

Abstract

Secondary ice production (SIP) modulates tropical convection, but its interactions with aerosol loading remain uncertain. Using the UK Met Office Unified Model with detailed SIP parameterizations, this study investigates how multiple SIP mechanisms affect a Hector storm under weak instability and varying cloud condensation nuclei (CCN) concentrations. At moderate aerosol loading (N_d = 400 cm^{-3}), SIP substantially enhances the ice phase. Ice number increases by over 3 orders of magnitude at temperatures warmer than –10 °C, and ice water content rises by up to ~120% in the anvil. SIP also reduces outgoing longwave radiation (OLR) by 6.8 W m^{-2} (–2.5%), increases outgoing shortwave radiation (OSR) by 7.9 W m^{-2} (+2%), over a 110 km × 110 km region in 6 hours. For this case, precipitation becomes more organized near the convective core, with total accumulation increasing by ~25%. Under polluted (N_d = 800 cm^{-3}) and clean (N_d = 200 cm^{-3}) conditions, SIP effects are weaker or spatially fragmented, indicating non-linear aerosol dependence. Sensitivity experiments show that, when combined with rime-splintering (RS), Mode 1 (droplet fragmentation during freezing) weakens at high CCN owing to reduced supercooled raindrop supply in the mixed-phase layer, while Mode 2 (drop–ice collisions with splashing) is inhibited at low CCN due to less encounters with large rimed ice particles. In contrast, RS and its combination with ice–ice collisional breakup show relatively limited aerosol sensitivity in this case.

https://doi.org/10.5194/egusphere-2025-5665
Preprint. Discussion started: 19 November 2025

1 Introduction

Tropical deep convection plays a central role in the global climate and hydrological cycle by regulating precipitation, radiation, and energy transport. The microphysical processes governing the development of these systems remain a major source of uncertainty in weather and climate models. In particular, the formation of ice in mixed-phase clouds is not fully explained by primary ice nucleation alone, as observed ice crystal number concentrations (ICNC) often exceed measured ice-nucleating particle (INP) concentrations by several orders of magnitude (e.g., Hobbs and Rangno, 1985; Ladino et al., 2017; Field et al., 2017). This discrepancy points to the importance of secondary ice production (SIP), whereby new ice particles are generated from pre-existing ones.

A range of SIP mechanisms has been identified, including rime-splintering (hereafter RS; Hallett and Mossop, 1974), collisional breakup of ice particles (hereafter BR; Vardiman, 1978; Grzegorczyk et al., 2023), and sublimation-induced fragmentation (Oraltay and Hallett, 1989). Droplet shattering during freezing has also been documented and is commonly classified into Mode 1 and Mode 2 based on the symmetry of freezing (Dye and Hobbs, 1968; Lauber et al., 2018; James et al., 2021). Laboratory experiments confirm that these processes can generate large numbers of new ice particles, while observations frequently report SIP signatures in both mid-latitude and tropical convection (Field et al., 2017; Korolev and Leisner, 2020; Huang et al., 2022). At the microphysical level, SIP substantially enhances ICNC and ice water content (IWC), and alters the phase distribution between liquid and ice (Phillips et al., 2017; James et al., 2023; Han et al., 2024).

At the storm scale, modeling and observational studies have shown that SIP can strongly influence cloud radiative and precipitation responses. By increasing anvil extent and optical depth, SIP modifies outgoing longwave radiation (OLR) and shortwave reflection (Young et al., 2019; Hawker et al., 2021a). At the same time, changes in riming and melting pathways modify rainfall intensity and organization. For instance, Han et al. (2024) reported that including SIP in central European convection increased ICNC by more than twentyfold and reduced surface precipitation by up to 20%. Grzegorczyk et al. (2025a) found that enabling SIP in a heavy-precipitation case improved agreement with in-situ ice measurements while reducing heavy rain occurrence. Dedekind et al. (2021) showed that in mid-latitude winter convection, SIP enhanced ICNC and surface precipitation, with impacts highly sensitive to the chosen parameterizations. In tropical convection, SIP has been associated with the maintenance of extensive anvils and changes in precipitation efficiency (Hawker et al., 2021b; Qu et al., 2022; Waman et al., 2022),

https://doi.org/10.5194/egusphere-2025-5665
Preprint. Discussion started: 19 November 2025

while in stratiform and Arctic mixed-phase clouds it helps explain persistent ICNC well above INP limits (Sotiropoulou et al., 2020; Zhao et al., 2021). Despite these advances, substantial uncertainties remain. Different SIP mechanisms dominate in different temperature ranges, their relative importance varies across environments, and parameterizations diverge among models (Field et al., 2017; Sullivan et al., 2018; Korolev and Leisner, 2020).

Beyond SIP itself, aerosol loading is expected to modulate its efficiency by reshaping hydrometeor properties in the mixed-phase region. In relatively clean air, collision–coalescence tends to occur earlier, accelerating warm-rain processes. This can increase the abundance of raindrops that participate in riming, but it also depletes the supercooled liquid aloft that sustains SIP (Rosenfeld and Woodley, 2000; Khain et al., 2005). With increasing cloud condensation nuclei (CCN), more numerous, smaller droplets delay autoconversion and loft more liquid above the freezing level, maintaining supercooled water and modifying droplet shattering and collisional breakup between ice particles (Rosenfeld et al., 2008; Qu et al., 2020). Which SIP route dominates therefore depends on temperature, the intensity of riming, and the availability of precipitation hydrometeors suitable for riming, implying a nonlinear dependence of SIP efficiency on aerosol loading (Fan et al., 2016; Grabowski and Morrison, 2020; Varble et al., 2023). Qu et al. (2020) showed that aerosol-controlled droplet spectra modulate SIP and the partition between liquid and ice, influencing storm evolution. Huang et al. (2025) linked CCN impacts to changes in SIP and subsequent storm electrification. However, most existing studies examine aerosol effects and SIP sensitivities separately. Systematic evaluations of aerosol–SIP interactions across CCN regimes, particularly in tropical convection, remain limited (e.g., Field et al., 2017; Korolev and Leisner, 2020).

This study addresses this gap by investigating how SIP interacts with CCN to influence cloud–precipitation–radiation processes in tropical convection. We focus on a weak-CAPE Darwin storm on 6 February 2006 and conduct sensitivity experiments with the Unified Model and CASIM microphysics across clean, moderate, and polluted CCN levels. In addition, we examine the CCN sensitivity of individual SIP mechanisms (RS, Mode 1, Mode 2, and BR), to clarify their relative contributions. Through this analysis, we aim to provide new insights into how SIP and aerosols jointly modulate tropical convection and storm evolution, and to emphasize the importance of representing SIP processes accurately in weather and climate models.

https://doi.org/10.5194/egusphere-2025-5665
Preprint. Discussion started: 19 November 2025

2 Method

2.1 Model description

The Met Office Unified Model (UM) vn13.0 with the Cloud AeroSol Interacting Microphysics Module (CASIM; Field et al., 2023) is used in this study. Simulations are conducted using the Regional Atmosphere and Land (RAL) 3.2 configuration (Bush et al., 2023). The UM employs the ENDGame non-hydrostatic dynamical core with a semi-Lagrangian formulation (Wood et al., 2014). Subgrid cloud fraction (and hence liquid condensation) is diagnosed with the bimodal cloud fraction scheme of van Weverberg et al. (2021), subgrid mixing in the boundary layer is represented by the Lock et al. (2000) scheme, and no convection parameterization is active. Further details are provided in Bush et al. (2025).

Cloud microphysics are represented using the CASIM scheme, configured in two-moment mode to prognostically predict both mass and number concentrations for five hydrometeor species: cloud droplets, raindrops, ice crystals, graupel, and snow. Particle size distributions follow a generalized gamma distribution. In CASIM, the cloud droplet number concentration (N_d) can be either prescribed as a fixed value or diagnosed from background aerosol. To systematically examine aerosol sensitivity and better control perturbations, we adopt the fixed N_d approach in this study. As in RAL3.2, a vertical taper is imposed on the fixed N_d to avoid unrealistically high droplet concentrations at upper levels and the associated excessive homogeneous freezing (Bush et al., 2025).

Rain is generated through auto-conversion, accretion, and melting of ice-phase particles, while losses include evaporation and freezing by ice. The separate treatment of mass and number concentrations allows for variability in hydrometeor size and fall speed, which directly affects sedimentation and evaporation. In contrast to single-moment schemes where particle size is fixed for a given mass, CASIM allows dynamic adjustment of size distributions based on aerosol and microphysical evolution.

Heterogeneous ice nucleation is parameterized using the default scheme of Cooper (1986), which prescribes ice crystal number concentrations as a function of temperature. Immersion freezing of raindrops is parameterized following Bigg (1953), with freezing probability depending on drop volume and temperature. When freezing occurs, rain mass and number are converted to graupel, providing a bulk representation of raindrop freezing in CASIM (Field et al., 2023; Miltenberger et al., 2020). Homogeneous freezing of cloud droplets occurs below –38 °C (Jeffery and Austin, 1997).

In addition to primary ice nucleation, this study incorporates multiple secondary ice production (SIP) mechanisms. The default SIP process in CASIM is rime-splintering (RS), which produces ice splinters

https://doi.org/10.5194/egusphere-2025-5665
Preprint. Discussion started: 19 November 2025

through the riming of supercooled droplets by graupel and snow between –2.5 °C and –7.5 °C, with peak efficiency at –5 °C (Hallett and Mossop, 1974; Mossop, 1985). The production rate is based on the cloud liquid accreted by graupel and snow, using a default efficiency of 350 ice splinters per milligram of rimed liquid. In our previous study (Sun et al., 2025), we implemented three additional SIP mechanisms into CASIM: ice-ice collisional breakup (BR), and droplet shattering during symmetrical and asymmetrical freezing (Mode 1 and Mode 2). The BR parameterization follows the theoretical formulation of Phillips et al. (2017), and accounts for collisions between ice-phase particles (graupel, snow, and ice crystals). The production rate depends on collision kinetic energy, rimed fraction, temperature, and particle size. For droplet shattering, we adopt the two-mode parameterization from Phillips et al. (2018). Mode 1 (M1) describes the collisions between frozen drops and smaller ice particles, with splinter numbers fitted to laboratory data using Lorentzian curves, peaking around –15 °C. Mode 2 (M2) involves collisions between freezing raindrops and more massive ice particles, where fragmentation is governed by the ratio of collision kinetic to surface energy. An empirical factor of 0.3, representing the ice-containing fraction of fragments, is applied following James et al. (2021).

Radiative transfer is handled by the SOCRATES scheme (Edwards and Slingo, 1996; Manners et al., 2023), which employs the two-stream approximation for fluxes and spherical harmonics for radiance. The single-scattering properties of ice crystals are derived from both the ice water content and the number concentration of ice-phase hydrometeors predicted by CASIM. This allows changes in ice particle characteristics associated with different SIP mechanisms to influence the simulated cloud optical properties. Turbulence is represented by the blended boundary layer scheme (Boutle et al., 2014), which incorporates both local and non-local mixing processes.

2.2 Model set-up and design of the simulations

Simulations were conducted for the 6 February 2006 case from the Aerosol and Chemical Transport in tropIcal convection (ACTIVE) campaign (Vaughan et al., 2008; Connolly et al., 2013). The ACTIVE campaign was carried out in the Darwin region of northern Australia and aimed to investigate aerosol-cloud interactions in tropical convection. This case, which occurred during the break period of the monsoon season, featured a relatively weaker convective storm over the Tiwi Islands (Figure 1a). In contrast to the vigorous pre-monsoon convection, the environment was characterized by a dry mid-troposphere and limited convective instability, with a convective available potential energy (CAPE) of approximately 1010 J kg^{-1} (Figure 1b).

https://doi.org/10.5194/egusphere-2025-5665
Preprint. Discussion started: 19 November 2025

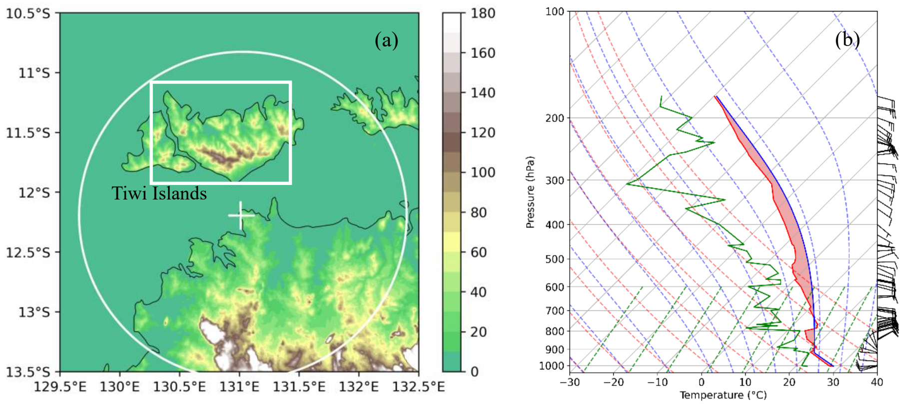

Figure 1. (a) Overview of model orography (terrain height, unit: m) and spatial domains used for radar and satellite data analysis (adapted from Sun et al., 2025). The full simulation domain is a 1350 km × 1350 km square centered at (12.4°S, 130.8°E). The subdomain used for radar evaluation and model diagnostic is indicated by the white box. The effective range of the CPOL radar, centered at (12.25°S, 131.05°E), is shown as the overlaid circle. (b) Atmospheric profiles from Darwin Airport station (12.42°S, 130.89°E) at 00 UTC on 6 February 2006. The green and red solid lines represent dew point and temperature, and the blue line represents the parcel lapse rate.

The cloud-resolving simulations are conducted at a horizontal resolution of 1.5 km, using a domain of 900 × 900 grid points centered over the Darwin region (12.4°S, 130.8°E). The vertical grid contains 90 levels, extending up to 40 km, with finer resolution in the lower atmosphere (52 levels below 10 km, 33 below 4 km, and 16 below 1 km). Each simulation starts at 18 UTC on 5 February 2006 and runs for 36 hours. Boundary and initial conditions are prescribed from the ECMWF Reanalysis version 5 (ERA5) reanalysis data, updated every 6 hours. A spin-up period of 6 hours is applied, with a model time step of 75 seconds. To better represent surface features, we incorporate the Shuttle Radar Topography Mission (SRTM; NASA, 2013) dataset as ancillary input. For analysis, we focus on a 1° × 1° subdomain over the Tiwi Islands (indicated by the white box in Figure 1a), selected to minimize potential boundary effects.

To investigate the sensitivity of mixed-phase convection to secondary ice production (SIP) mechanisms and aerosol conditions, a series of simulations was conducted combining different CCN concentrations with various SIP configurations (Table 1). For CCN, we employed a fixed in-cloud droplet number concentrations (N_d) approach, allowing a more controlled evaluation of microphysical and radiative responses to SIP processes. N_d was specified at three representative levels: 200, 400, and 800 cm^{-3}, corresponding to low, moderate, and high aerosol loading. These values are within the range

https://doi.org/10.5194/egusphere-2025-5665
Preprint. Discussion started: 19 November 2025

observed over the tropical maritime region and are broadly consistent with previous modeling studies (e.g., Connolly et al., 2013).

For each N_d value, six SIP scenarios were tested: all SIP mechanisms active (all-SIP), no SIP process enabled (no-SIP), riming-splintering only (RS), and three combined schemes involving RS with one additional mechanism: RS with Mode 1 (RS+M1), RS with Mode 2 (RS+M2), and RS with ice–ice collisional breakup (RS+BR). This design enables a systematic assessment of how aerosol conditions influence the impact of individual SIP processes on cloud microphysics, radiation, and precipitation.

2.3 Observational data

The modeled reflectivity fields were evaluated against observations from the C-band polarimetric radar (CPOL), located at Gunn Point (12.25°S, 131.05°E). The CPOL radar provides volumetric scans every 10 minutes, with a vertical resolution of 0.5 km and horizontal resolution of 2.5 km. To facilitate comparison with the model, we used the Statistical Coverage Product (May et al., 2009), which represents the time–height distribution of the fraction of a defined domain exceeding 10 dBZ, a threshold chosen to capture the spatial and temporal characteristics of convective precipitation. The analysis domain is indicated in Figure 1a.

Simulated rainfall accumulations were also compared against CPOL radar–derived precipitation datasets, available at 10-minute intervals and 1 km horizontal resolution. Despite residual uncertainty may arise from reflectivity calibration and C-band attenuation, CPOL quantitative precipitation estimates generally provide a reliable representation of tropical rainfall (Louf et al., 2019; Jackson et al., 2021). Radiosonde profiles from Darwin Airport station (12.42°S, 130.89°E) were used to characterize the thermodynamic environment. Additionally, top-of-atmosphere radiation was evaluated using equivalent outgoing longwave radiation (OLR) calculated from Multifunctional Transport Satellites (MTSAT) brightness temperature, with spatial and temporal resolutions of 1.25 km and 30 minutes, respectively.

3 Results

3.1 SIP impacts on radiation under varying CCN conditions

Figure 2 shows the spatial distribution of outgoing longwave radiation (OLR) from three model simulations (allSIP-200, allSIP-400, and allSIP-800) and their comparison with observations. On 6 February 2006, the Hector storm developed over the Tiwi Islands during the break period of the monsoon

https://doi.org/10.5194/egusphere-2025-5665
Preprint. Discussion started: 19 November 2025

season. MTSAT visible imagery (Figures 2a–c) shows that shallow cumulus initiated along the sea-breeze front (Connolly et al., 2013). Between 07:30 and 08:30 UTC, these shallow clouds rapidly developed, with the system reaching maturity by 09:30 UTC. The coldest cloud tops, corresponding to minimum OLR values below 150 W m^{-2}, were concentrated over central island with an expanding westward anvil.

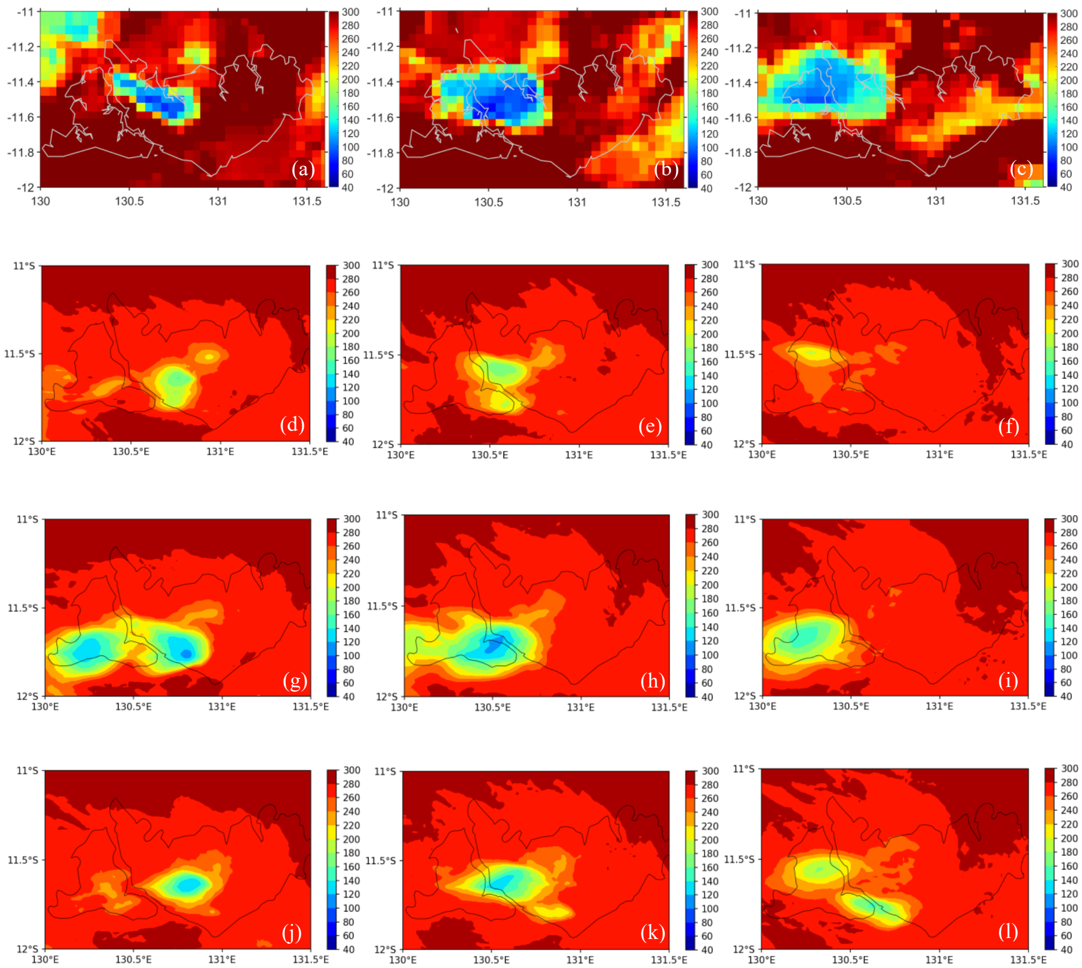

Figure 2. Spatial distribution of MTSAT visible channel imagery at (a) 07:30, (b) 08:30 and (c) 09:30 UTC on 6 February 2006, and outgoing longwave radiation (OLR; W m^{-2}) from allSIP simulations for (d–f) N_d = 200 cm^{-3}, (g–i) N_d = 400 cm^{-3}, and (j–l) N_d = 800 cm^{-3} at 06:30, 07:30, and 08:30 UTC, respectively. N_d denotes the prescribed in-cloud droplet number concentration. Simulation times are shifted by –1 h to match the earlier convection development in the model. Equivalent plots for simulated noSIP cases are provided in Figure S1 in the Supplement.

https://doi.org/10.5194/egusphere-2025-5665
Preprint. Discussion started: 19 November 2025

The simulated convection evolution and anvil expansion are broadly consistent with satellite observations. The impacts of SIP on radiation were first examined through the spatial distribution of OLR of noSIP at 07:30 UTC (Figure S1 in the Supplement). Under moderate aerosol loading (N_d = 400 cm^{-3}), the allSIP simulation produces a minimum OLR of ~150 W m^{-2} (Figure 2h), about 25 W m^{-2} lower than in the noSIP case (~175 W m^{-2}), and expands the area with OLR < 200 W m^{-2} by around 25–30% (Figure S1e). In contrast, for low aerosol loading (N_d = 200 cm^{-3}), the allSIP case shows a weaker enhancement compared to the noSIP, with a minimum OLR of ~165 W m^{-2} and a smaller increase in the low-OLR coverage (~10–15%; Figures 2e, S1b). At high aerosol loading (N_d = 800 cm^{-3}), the allSIP run still exhibits reduced OLR relative to noSIP, but the low-OLR region becomes more fragmented (Figures 2k, S1h).

The CFADs (contoured frequency by altitude diagrams) of reflectivity (>10 dBZ), as shown in Figure 3, further link these radiative patterns to storm structure. For N_d = 400 cm^{-3}, the allSIP case sustains a broader vertical extent of high reflectivity above 10 km (Figure 3b), indicating stronger convection that supports the formation of extensive anvil clouds, consistent with the expanded low-OLR region. In the N_d = 200 cm^{-3} case, the reflectivity enhancement is weaker and confined to mid-levels, explaining the smaller radiative impact (Figures 2d–f). At N_d = 800 cm^{-3}, high reflectivity reaches upper levels (Figure 3f), but these echoes are more vertically dispersed and occur with lower frequency at each height compared to N_d = 400 cm^{-3}. This suggests a broader yet optically thinner distribution of hydrometeors, which may explain the less concentrated low-OLR region (Figures 2j–l). Overall, N_d = 400 cm^{-3} shows a better agreement with the observation. allSIP produces stronger convection than noSIP when N_d = 400 and 800 cm^{-3}, while the difference is minimal at N_d = 200 cm^{-3}.

The temporal evolution of domain-averaged OLR further illustrates these effects (Figure 4a and Table 2). In all simulations, OLR decreases after 02:00 UTC as convection develops, reaching minima around 06:00 UTC before recovering to ~278 W m^{-2} by the end of the simulation. The inclusion of SIP systematically reduces OLR relative to noSIP runs, consistent with stronger anvil development and enhanced upper-level ice content. The strongest reduction occurs at moderate aerosol loading (N_d = 400 cm^{-3}), where OLR drops below 250 W m^{-2} and the mean SIP–noSIP difference reaches –6.86 W m^{-2} (–2.5%). Under clean conditions (N_d = 200 cm^{-3}), SIP yields a slight increase of +0.61 W m^{-2} (+0.2%), whereas under polluted conditions (N_d = 800 cm^{-3}) it leads to a small decrease of –3.34 W m^{-2} (–1.2%). In contrast, outgoing shortwave radiation (OSR; Figure 4b) increases after 02:00 UTC and peaks around 06:00 UTC, but its response to SIP is more variable. At N_d = 400 cm^{-3}, SIP enhances OSR relative to

https://doi.org/10.5194/egusphere-2025-5665
Preprint. Discussion started: 19 November 2025

noSIP, with peak values exceeding 500 W m^{-2} compared to ~480 W m^{-2}, and a mean increase of +7.95 W m^{-2} (+2.0%). At N_d = 200 cm^{-3}, however, SIP reduces OSR by –6.55 W m^{-2} (–1.8%), while at N_d = 800 cm^{-3} the reduction is smaller at –4.05 W m^{-2} (–0.9%). This contrast suggests that SIP has a robust and consistent impact on longwave radiation by maintaining colder, more extensive anvils, whereas its shortwave effect is weaker and dependent on CCN concentration. In addition, OSR differences may be further influenced by variations in cloud phase, particle size, and the timing of solar insolation (Yin and Porporato, 2017).

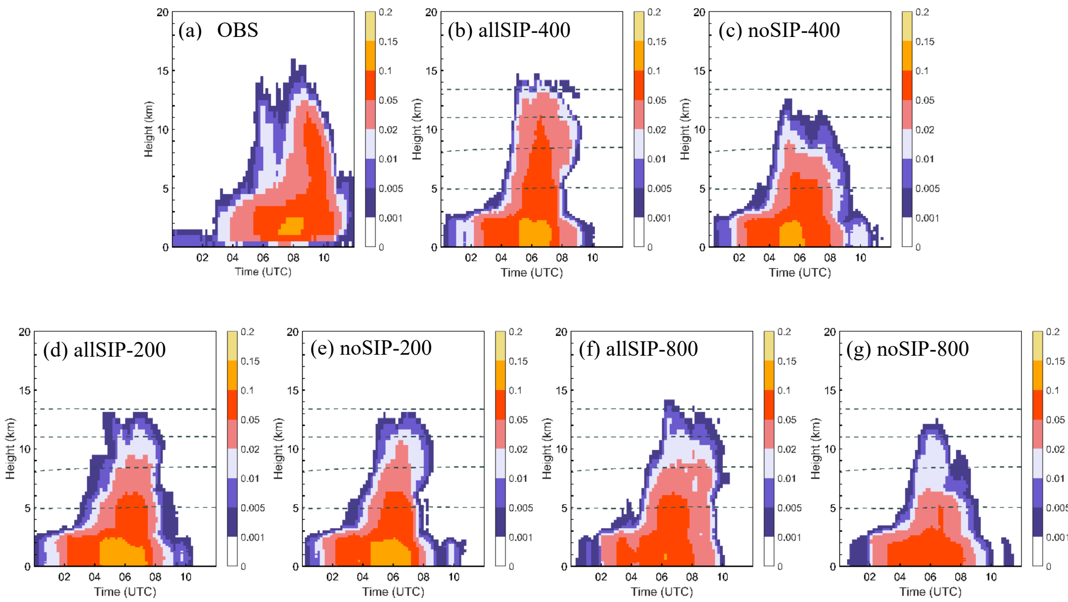

Figure 3. Time-height plots of CFADs (contoured frequency by altitude diagrams) for radar reflectivity greater than 10 dBZ from (a) CPOL observation, (b) allSIP-400, (c) noSIP-400, (d) allSIP-200, (e) noSIP-200, (f) allSIP-800, and (g) noSIP-800 simulations. The 0, –20, –40, and –60 °C isotherms are indicated by dashed lines in panels (b)-(g).

https://doi.org/10.5194/egusphere-2025-5665
Preprint. Discussion started: 19 November 2025

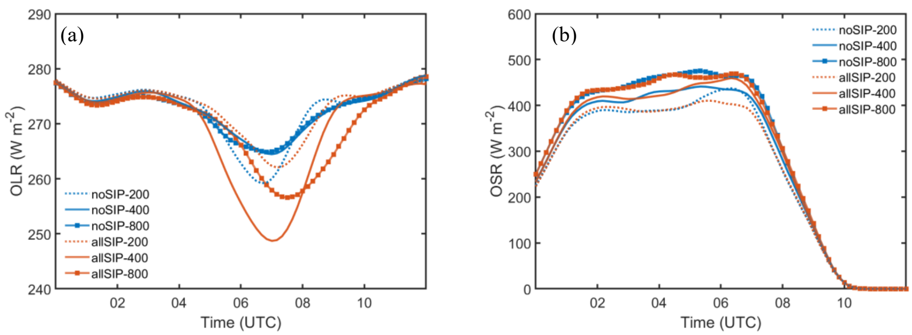

Figure 4. Time series of domain-averaged (a) outgoing longwave radiation (OLR) and (b) outgoing shortwave radiation (OSR) based on simulations. Dotted lines denote $N_d = 200$ cm^{-3}, solid lines denote $N_d = 400$ cm^{-3}, and solid lines with square markers denote $N_d = 800$ cm^{-3}.

3.2 SIP impacts on precipitation under varying CCN conditions

The spatial distribution of accumulated precipitation from 04:00–10:00 UTC (Figure 5) shows that SIP affects both the intensity and organization of rainfall, with responses depending on CCN concentrations. In the allSIP-400 simulation, the rainband structure and heavy rainfall cores (> 100 mm) align more closely with CPOL observations than in noSIP-400 (Figures 5a–c), suggesting that SIP-induced ice enhancement strengthens convection and promotes greater organization. At $N_d = 200$ cm^{-3} (Figures 5d–e), the inclusion of SIP slightly increases the number of rainfall cores but does not substantially change the overall coverage compared to noSIP-200, indicating that the additional ice-phase growth does not strongly affect the convective system in clean conditions. Under $N_d = 800$ cm^{-3} (Figures 5f–g), SIP broadens the precipitation area but produces more fragmented rainfall spots than at 400 cm^{-3}, resembling the more dispersed pattern in the OLR distribution (Figures 2k–l).

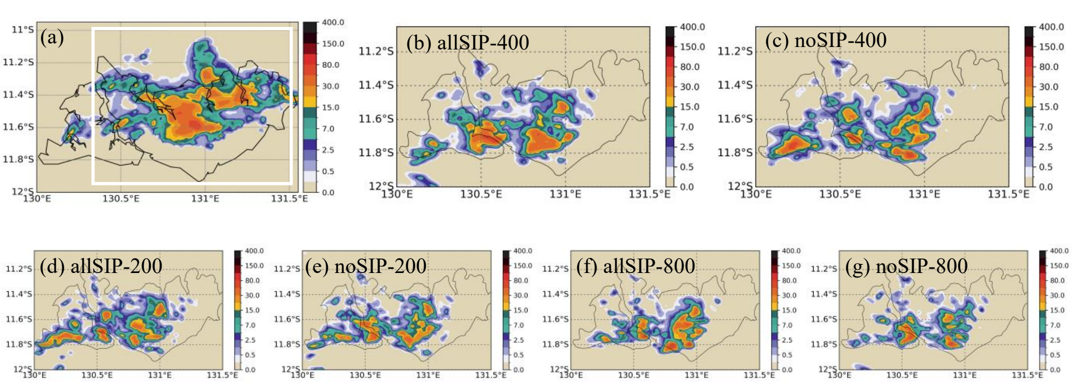

https://doi.org/10.5194/egusphere-2025-5665
Preprint. Discussion started: 19 November 2025

Figure 5. Spatial distribution of accumulated precipitation (mm) during 04:00–10:00 UTC on 6 February 2006 from (a) CPOL observations and simulations for (b) allSIP-400, (c) noSIP-400, (d) allSIP-200, (e) noSIP-200, (f) allSIP-800, and (g) noSIP-800.

Domain-averaged precipitation time series (Figure 6) further quantify these effects. In allSIP-400, the peak precipitation rate (~1.35 mm h^{-1}) is closer in timing and magnitude to observations than in other runs. It is also notably higher than noSIP-400 (~0.80 mm h^{-1}; Figure 6a). With moderate aerosol loading, SIP enhances the production of ice-phase particles aloft, accelerating mixed-phase processes (Sun et al., 2025). This promotes melting and sustains a robust rain region, as shown in Figure 5b. For N_d = 200 cm^{-3}, allSIP (~0.95 mm h^{-1}) produces a lower peak rate than noSIP (~1.20 mm h^{-1}). In clean conditions, warm-rain processes dominate early precipitation formation via efficient collision–coalescence. SIP accelerates glaciation, shifting water mass from the liquid to the ice phase during the early storm stage, reducing the efficiency of warm-rain production and suppressing peak rates. The precipitation duration remains comparable, resulting in similar accumulated totals between allSIP-200 (~3.25 mm) and noSIP-200 (~3.27 mm; Figure 6b). For N_d = 400 cm^{-3}, allSIP (~3.54 mm) yields a higher accumulated total than noSIP (~2.81 mm, +25%; Figure 6b), consistent with its stronger precipitation peak and better agreement with observations. At N_d = 800 cm^{-3}, high aerosol loading delays precipitation onset due to smaller cloud droplet sizes and reduced collision–coalescence efficiency. SIP in this condition increases ice water content, leading to greater late-stage precipitation in allSIP-800 than in noSIP-800 (~2.30 mm). However, the total accumulation in allSIP-800 (~3.11 mm) remains lower than in allSIP-400 (~3.54 mm), as the limited warm-rain formation under high droplet number concentrations cannot be fully compensated by the enhanced ice-phase process. Across all simulations, the accumulated precipitation remains lower than observations, including the allSIP-400 case, which shows the best agreement (Figure 6b). Notably, the domain totals span ~50% across the combinations of SIP and N_d (2.30–3.54 mm), underscoring their important control on accumulation. This provides a clear motivation to represent and constrain these processes with observations to improve rainfall prediction.

https://doi.org/10.5194/egusphere-2025-5665
Preprint. Discussion started: 19 November 2025

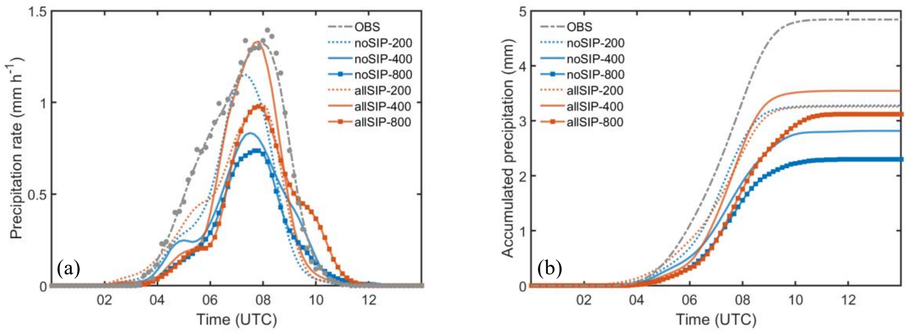

Figure 6. Time series of domain-averaged (a) precipitation rate (mm h^{-1}) and (b) accumulated precipitation (mm) from CPOL observations (OBS; gray dash-dot) and simulations without SIP (noSIP; blue) and with all SIP mechanisms activated (allSIP; red) for N_d = 200 cm^{-3} (dotted lines), N_d = 400 cm^{-3} (solid lines), and N_d = 800 cm^{-3} (solid lines with square markers). The gray dashed line in panel (a) represents a fitted curve to the observations. For comparison, the time axis of the simulations has been shifted by –1 h to align with the observations.

Overall, these results suggest that SIP can intensify rainfall and produce a more concentrated precipitation pattern, particularly under moderate aerosol conditions (N_d = 400 cm^{-3}). Under low aerosol loading, large cloud droplets allow warm-rain processes to occur efficiently even without SIP, so the additional ice-phase pathway has only a small impact on precipitation. Under high aerosol loading, enhanced cloud droplet numbers delay warm-rain processes and lead to more dispersed precipitation; SIP increases totals relative to noSIP but cannot match the allSIP-400 case.

3.3 SIP impacts on cloud microphysics under varying CCN conditions

3.3.1 Microphysics associated with radiation and precipitation responses

To interpret the radiative and precipitation responses presented in previous sections, we examine the vertical structures of key hydrometeors under different CCN and SIP conditions (Figure 7). These include cloud droplets, raindrops, ice crystals, and graupel, ice water content (IWC), and updraft strength.

Cloud droplet number concentration increases with CCN levels as expected, ranging from ~0.5 × 10^8 m^{-3} at N_d = 200 cm^{-3} to over 2.0 × 10^8 m^{-3} at N_d = 800 cm^{-3} (Figure 7a). The mean-mass radius of cloud droplets decreases with increasing N_d (Figure 7f). The influence of SIP on cloud droplets is negligible compared to the dominant role of CCN.

https://doi.org/10.5194/egusphere-2025-5665
Preprint. Discussion started: 19 November 2025

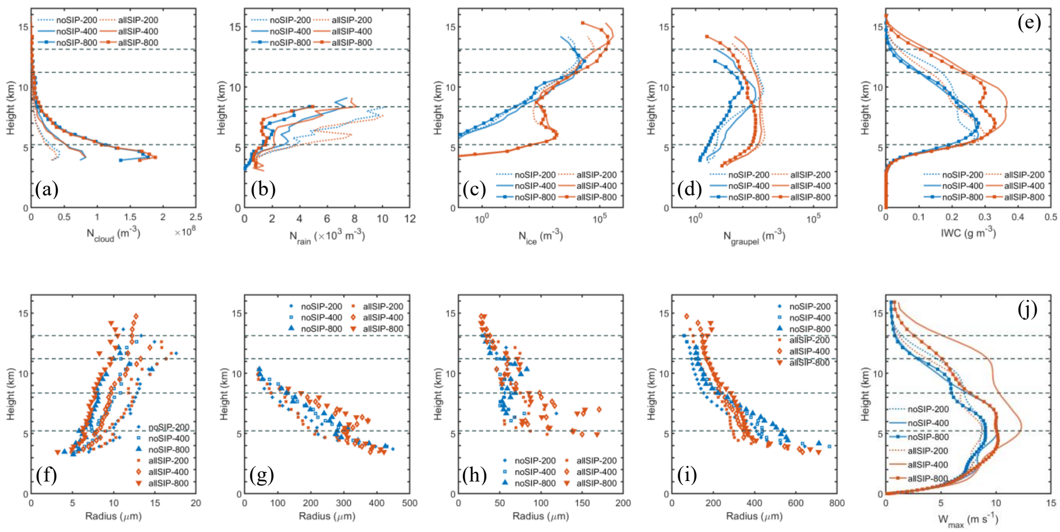

Figure 7. Vertical profiles of horizontally averaged microphysical and dynamical properties from simulations without SIP (noSIP) and with all SIP mechanisms (allSIP), under three CCN concentrations (N_d = 200, 400, and 800 cm^{-3}). Panels (a–d) show number concentrations of cloud droplets, rain, ice crystals, and graupel, respectively. Panels (f–i) show the corresponding mean-mass radii. Panels (e) and (j) display the ice water content (IWC, sum of ice crystals, graupel, and snow) and 95th percentile updraft velocity (W_{max}), used as a proxy of maximum updraft strength. Panels (a–b, f–g) are averaged over regions where either the ice water path or rain water path exceeds 1 g m^{-2}, while panels (c–e, h–j) are averaged over regions where IWC > 0.01 g m^{-3} during 02:30–08:30 UTC on 6 February 2006. In panels (a–e, j), dotted lines denote N_d = 200 cm^{-3}, solid lines denote N_d = 400 cm^{-3}, and solid lines with square markers denote N_d = 800 cm^{-3}. Gray dashed lines indicate the 0, −20, −40, and −60 °C isotherms.

SIP leads to substantial enhancement in ice crystal number concentration (N_{ice}; Figure 7c) between 5 and 9 km, especially at N_d = 400 cm^{-3}. At 5–7 km, allSIP-400 reaches ~3×10^3 m^{-3}, more than three orders of magnitude higher than noSIP-400. AllSIP-800 shows a similar enhancement in this layer, but the increase is more vertically dispersed, with a secondary peak (~0.5×10^3 m^{-3}) near 8 km, comparable to allSIP-400. In the clean case (N_d = 200 cm^{-3}), N_{ice} enhancement is confined below 7 km, and values between 7–9 km are roughly half those in the 400 and 800 cm^{-3} cases (~0.2 × 10^3 m^{-3}). Ice crystal radius (Figure 7h) also increases in allSIP simulations. At ~7 km, allSIP-400 reaches > 100 μm, compared to ~60 μm in noSIP-400. In contrast, noSIP cases show little variation in radius across CCN levels between 5–9 km. This suggests that SIP not only increases ice particle numbers but also supports their growth via vapor deposition. Radius increases are also seen in allSIP-800, though less pronounced than at 400 cm^{-3}.

https://doi.org/10.5194/egusphere-2025-5665
Preprint. Discussion started: 19 November 2025

At 200 cm^{-3}, the radius difference between allSIP and noSIP is minimal, reflecting weaker updrafts and limited condensate under low-CCN conditions.

Graupel number concentration ($N_{graupel}$) is also enhanced by SIP across all CCN levels (Figure 7d). The largest increase occurs at N_d = 200 and 400 cm^{-3}, where allSIP simulations reach ~10^3 m^{-3} near 6 km, compared to ~10 m^{-3} in the corresponding noSIP runs. At N_d = 800 cm^{-3}, the enhancement is smaller, consistent with previous findings that polluted conditions suppress graupel formation by delaying raindrop freezing (Sun et al., 2021, 2024). The graupel radius decreases under SIP at all CCN levels (Figure 7i). For example, at ~5.5 km, graupel radius in allSIP-200 is ~300 µm, compared to ~400 µm in noSIP-200, likely due to enhanced competition for supercooled liquid among more numerous graupel particles. Across the SIP experiments, diagnosed snow exhibits only small changes relative to crystals and graupel, indicating a limited sensitivity to SIP in this case, consistent with a separate Hector simulation with CASIM (e.g., Sun et al., 2025). Therefore, we do not discuss snow here.

Together, increases in ice crystal and graupel raise total ice water content (IWC) and the associated latent heating. SIP enhances the IWC most significantly at N_d = 400 cm^{-3}, where allSIP-400 exceeds 0.35 g m^{-3} above 7 km, compared to ~0.25 g m^{-3} in noSIP-400 at the same altitude (Figure 7e). Near 10 km, allSIP-400 shows a maximum enhancement of +121.7% relative to noSIP (Table 2). At N_d = 800 cm^{-3}, the response is weaker and more vertically dispersed, with peaks near 7 km and 10 km and a maximum difference of +0.16 g m^{-3} (+87.9%) around 10 km. At N_d = 200 cm^{-3}, the IWC difference between allSIP and noSIP is minimal, despite increases in N_{ice} and $N_{graupel}$. Because warm-rain processes dominate in clean air, supercooled liquid available for riming and deposition is depleted, limiting mass growth. As a result, IWC changes remain negligible and the allSIP–noSIP updraft differences are small (Figure 7j). By contrast, at N_d = 400 and 800 cm^{-3}, SIP produces larger and more persistent IWC aloft (Figures 7e). The latent heating from freezing strengthens mid- to upper-level updrafts by 2–4 m s^{-1} relative to noSIP (Figure 7j). Stronger updrafts transport more cloud water to upper levels, sustaining further SIP and depositional growth. In this study, total IWC is defined as the sum of all ice-phase species (ice crystals, graupel, and snow). While species diagnostics focus on crystals and graupel because they exhibit clearer SIP signals, snow is retained in IWC to provide a physically consistent measure of total ice mass relevant to radiation and reflectivity.

Time–height cross sections (Figure 8) clarify how SIP modifies vertical cloud structure across aerosol conditions. IWC increases occur primarily above the melting level (~5 km) during 04:00–08:30 UTC (Figures 8a–f). The response is strongest at N_d = 400 cm^{-3}, with deeper anvils and longer persistence

https://doi.org/10.5194/egusphere-2025-5665
Preprint. Discussion started: 19 November 2025

(Figures 8b, 8e), consistent with the maxima in Figure 7e. At $N_d = 800$ cm^{-3}, enhancement is weaker and delayed relative to $N_d = 400$ cm^{-3} (Figures 8c, 8f), which helps explain the weaker OLR suppression. At $N_d = 200$ cm^{-3}, the difference between allSIP and noSIP is small and short-lived (Figures 8a, 8d), reflecting limited mass growth. Difference panels (Figures 8g–i) place the SIP-induced IWC increase mainly at mid- to upper levels (~7–13 km), peaking at $N_d = 400$ cm^{-3} (Figure 8h). At $N_d = 200$ cm^{-3}, changes are minimal or negative (Figure 8g), indicating weak SIP impact in clean air.

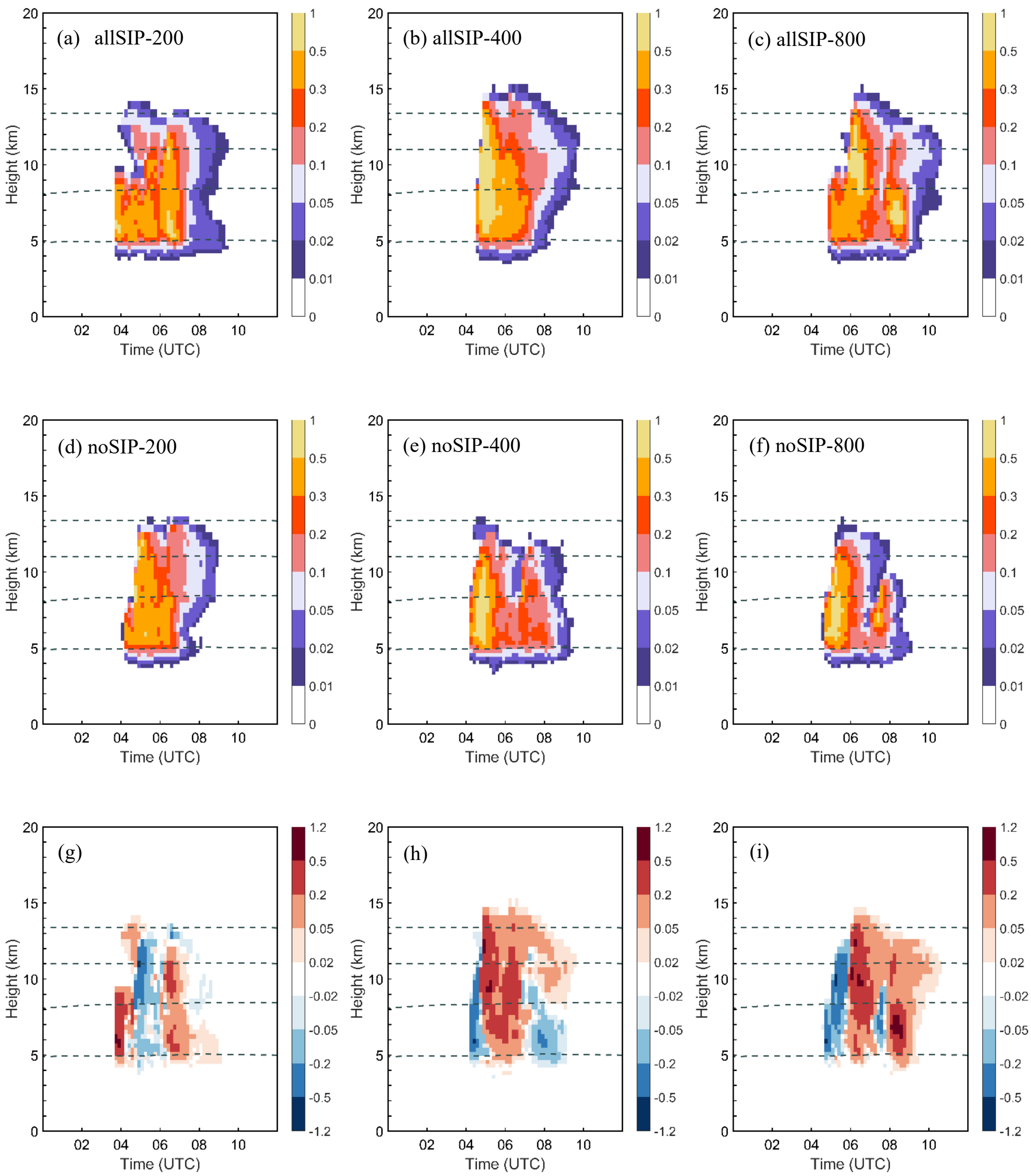

https://doi.org/10.5194/egusphere-2025-5665
Preprint. Discussion started: 19 November 2025

Figure 8. Time–height cross sections of ice water content (IWC; g m^{-3}) for simulations with all SIP mechanisms included: (a) allSIP-200, (b) allSIP-400, and (c) allSIP-800; and without SIP: (d) noSIP-200, (e) noSIP-400, and (f) noSIP-800. Panels (g–i) show the differences between allSIP and noSIP simulations at each CCN concentration (N_d = 200, 400, 800 cm^{-3}; i.e., allSIP minus noSIP). Panels (a–f) are averaged over regions where IWC > 0.01 g m^{-3}. The 0, −20, −40, and −60 °C isotherms are shown by the dashed lines. Corresponding plots for rain water content (RWC) are shown in Figure S2 in the Supplement.

SIP alters the vertical distribution of raindrops, and its impact varies with CCN levels. First, raindrop number concentration (N_{rain}) decreases from N_d = 200 to 800 cm^{-3} (Figure 7b), consistent with reduced warm-rain efficiency at higher CCN. Near the melting level (~4–5 km), N_{rain} is controlled primarily by CCN and shows negligible differences between allSIP and noSIP at each CCN. Below 4 km, however, N_{rain} is higher in allSIP than in noSIP for all CCN, indicating that melting of SIP-generated ice supplies additional raindrops to the lower altitudes. Above 5 km, SIP increases N_{rain} at N_d = 200 cm^{-3} but decreases it at N_d = 400 and 800 cm^{-3}. In clean air (N_d = 200 cm^{-3}), N_{rain} at 5–7 km exceeds that in the noSIP case, implying that weaker updrafts allow earlier melting of the limited SIP-produced ice aloft. In contrast, at N_d = 400 and 800 cm^{-3}, N_{rain} is reduced relative to the noSIP case above 5 km, because SIP generates numerous small ice particles that are retained by stronger updrafts and remain frozen, limiting raindrop formation at upper levels. For raindrop size (Figure 7g), radii are nearly identical below 5 km across CCN and between SIP and noSIP runs, indicating that mixing, coalescence, and evaporation tend to homogenize drop sizes at low levels. Above 5 km, radii are smallest at N_d = 200 cm^{-3} and larger at N_d = 400 and 800 cm^{-3}. SIP reduces mean radius at 5–7 km in the clean case (N_d = 200 cm^{-3}), with allSIP-200 reaching < 160 μm compared to ~200 μm in noSIP-200. This likely reflects a higher N_{rain} with little change in rainwater content, reducing the mean mass per drop and thus the radius. At N_d = 400 and 800 cm^{-3}, the raindrop size is larger in allSIP than in noSIP by ~30–100 μm above 5 km, suggesting that enhanced melting of ice particles converts water into fewer but larger raindrops.

Time–height sections of rainwater content (RWC) corroborate this pathway. At N_d = 400 cm^{-3}, SIP produces a pronounced RWC enhancement at ~3–6 km from ~04:00–06:00 UTC (Figure S2b in the Supplement), followed by a near-surface (0–2 km) RWC peak around ~06:30 UTC that coincides with the precipitation-rate maximum (Figure 6a). At N_d = 800 cm^{-3}, RWC is weaker overall and delayed (~05:00 UTC) relative to N_d = 400 cm^{-3}, consistent with aerosol-induced suppression and timing shifts. Nevertheless, allSIP-800 exceeds noSIP-800 (Figures S2c, S2f, S2i), suggesting that SIP still enhances

https://doi.org/10.5194/egusphere-2025-5665
Preprint. Discussion started: 19 November 2025

rainwater through melting of its generated ice particles under polluted conditions. At $N_d = 200$ cm^{-3}, RWC differences are minimal or negative especially between 04:00–06:00 UTC (Figure S2g), consistent with the limited IWC growth and the weak SIP influence on rainwater mass in clean air.

3.3.2 Sensitivity to individual SIP mechanisms

We examine how different secondary ice production pathways, namely allSIP, RS, RSM1, RSM2, and RSBR, modify the storm relative to the corresponding noSIP simulations at $N_d = 200$, 400, and 800 cm^{-3}, as shown in Figures 7 and 9. Diagnostics are expressed as height-dependent enhancements over noSIP (e.g., $\Delta IWC = IWC_{SIP} - IWC_{noSIP}$; see Table 3).

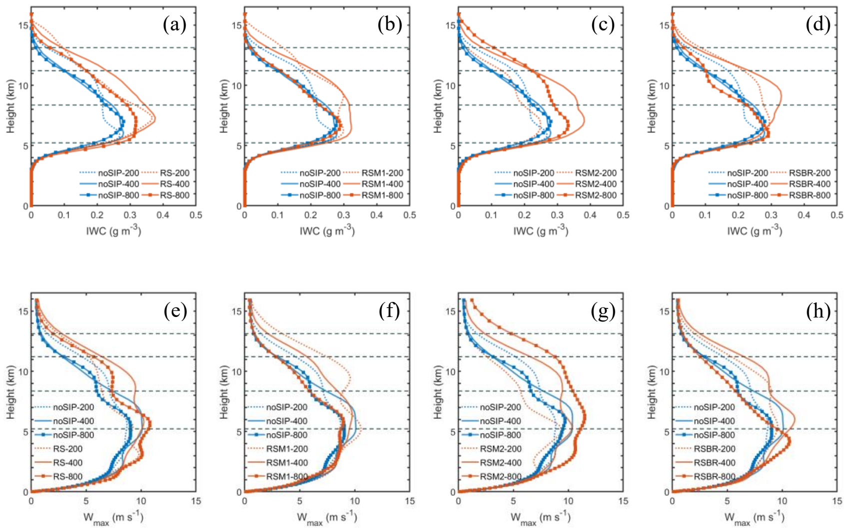

Figure 9. Vertical profiles of horizontally averaged (a-d) ice water content (IWC) and (e-h) 95th percentile updraft velocity (W_{max}) from simulations without SIP (noSIP) and with different SIP configurations: (a, e) RS, (b, f) RSM1, (c, g) RSM2, and (d, h) RSBR. Dotted lines denote $N_d = 200$ cm^{-3}, solid lines denote $N_d = 400$ cm^{-3}, and solid lines with square markers denote $N_d = 800$ cm^{-3}. All profiles are averaged over regions with IWC > 0.01 g m^{-3} during 02:30–08:30 UTC on 6 February 2006. Gray dashed lines indicate the 0, −20, −40, and −60 °C isotherms.

At the case level with all mechanisms active, SIP substantially increases IWC, with the largest enhancement at $N_d = 400$ cm^{-3}. The maximum ΔIWC reaches about +0.19 g m^{-3} (+121.7%), and the IWC maximum is close to 10 km (Figure 7e and Table 3). The peak updraft shows the same nonmonotonic dependence on CCN. W_{max} attains 12.6 m s^{-1} at $N_d = 400$ cm^{-3}, compared with 9.1 and 10.5 m s^{-1} at $N_d = 200$ and 800 cm^{-3} respectively (Figure 7j). The altitude of W_{max} is higher at $N_d = 400$ cm^{-3}, around 5.5

to 7 km, and lower in the clean and polluted cases (Table 3).

The CCN sensitivity of ΔIWC depends on the mechanism. RSM1 peaks at N_d = 400 cm^{-3} with +0.12 g m^{-3} (+78.1%), remains moderate at N_d = 200 cm^{-3} with +0.10 g m^{-3} (+47.4%), and becomes weak at N_d = 800 cm^{-3} with +0.03 g m^{-3} (+14.1%; Figure 9b). RSM2 also peaks at N_d = 400 cm^{-3} with +0.17 g m^{-3} (+109.7%), reduces to +0.08 g m^{-3} (+44.1%) at N_d = 800 cm^{-3}, and is weakest at N_d = 200 cm^{-3} with +0.03 g m^{-3} (+16.4%; Figure 9c). RS and RSBR produce large enhancements at N_d = 200 and 400 cm^{-3}, approximately +0.13–0.16 g m^{-3} (+85–106%), but weaker responses at N_d = 800 cm^{-3}, approximately +0.06–0.08 g m^{-3} (+29–40%; Figures 9a, d, and Table 3).

CCN also modulates the altitude of the SIP-induced maxima (Figure 9 and Table 3). For RSM1, the altitude of the ΔIWC maximum shifts from about 10 km at $N_d \leq$ 400 cm^{-3} to about 6 km at N_d = 800 cm^{-3}. For RSM2, the maximum remains near 10 km at $N_d \geq$ 400 cm^{-3} but lowers to about 7 km at N_d = 200 cm^{-3}. For RS and RSBR, the peak rises from about 7 km at N_d = 200 cm^{-3} to about 10 km at N_d = 400 cm^{-3}. These vertical shifts are consistent with the stronger upper-level ice in the N_d = 400 cm^{-3} case and the weaker enhancement under polluted conditions, which helps explain the CCN dependence of the OLR reduction. Peak updraft response is weaker than the IWC response, with ΔW_{max} rarely exceeding 1.5 m s^{-1}, and the largest W_{max} occurring at N_d = 400–800 cm^{-3} for RS, at N_d = 200 cm^{-3} for RSM1, at N_d = 800 cm^{-3} for RSM2, and at N_d = 400 cm^{-3} for RSBR (Figures 9e–h).

Microphysical diagnostics provide further detail. As shown in Figure 10, for RS and RSBR, ice crystal number concentrations exhibit evident peaks (>10^3 m^{-3}) between 5 and 8 km, and the three CCN profiles are nearly overlapping, indicating limited aerosol sensitivity. In the same layer, ice crystal mean-mass radii range from ~50–120 μm and show little variation with CCN (Figures 10e, h). For RSM1, the three CCN profiles are close together between 5 and 7 km, while between 7 and 9 km the N_d = 800 cm^{-3} case is clearly weaker than the N_d = 200 and 400 cm^{-3} cases. RSM1 produces the largest crystal radii among the mechanisms, often ~150–200 μm between 5 and 9 km, but these radii are nearly invariant with CCN. To test whether the suppression of RSM1 under polluted conditions arises from limited raindrop supply, we examine vertical profiles of cloud droplet and raindrop properties (Figures S3–S4 in the Supplement), focusing on number concentrations and mean-mass radii from about 0 to −20 °C, corresponding to about 5–9 km in these simulations. As shown in Figure S3, cloud droplets are primarily controlled by CCN rather than by the SIP configuration. Number concentrations increase from N_d = 200 to 800 cm^{-3}, whereas mean-mass radii decrease with CCN. In contrast, differences between RSM1 and noSIP are minor compared with the CCN effect. The prevalence of numerous but smaller droplets under

https://doi.org/10.5194/egusphere-2025-5665
Preprint. Discussion started: 19 November 2025

high CCN (Figure S3) is consistent with slower collision–coalescence and delayed growth toward raindrop sizes, implying a source limitation for Mode 1 in the 0 to −20 °C layer. Raindrop fields show the corresponding signature for RSM1 (Figure S4). Between 5–7 km, raindrop number concentration decreases with CCN, with the ordering $N_d = 200 > 400 > 800$ cm^{-3}, while the radius is largest at $N_d = 400$ cm^{-3}, smaller at $N_d = 800$ cm^{-3}, and smallest at $N_d = 200$ cm^{-3}. Between 7–9 km, the number concentration retains the same ordering, and the radius at $N_d = 400$ and 800 cm^{-3} is similar and both exceed that at $N_d = 200$ cm^{-3} (Figure S4). The larger radii above 5 km at $N_d = 400$ and 800 cm^{-3} are consistent with the concentration of available liquid into fewer drops at higher levels and may be aided by the melting of ice-phase hydrometeors. Taken together, these patterns indicate that polluted conditions do not favor the availability of the supercooled raindrops required by Mode 1. Although raindrops are similar or larger at higher levels for $N_d = 800$ cm^{-3}, their number and residence time in this layer are reduced, so the frequency of Mode 1 is lower. The reduced raindrop supply at $N_d = 800$ cm^{-3} also aligns with the weaker RSM1 ice production between 7–9 km (Figure 10) and with the minimum ΔIWC reported for RSM1 at high CCN (Table 3). Collectively, these diagnostics support the interpretation that the suppression of RSM1 under polluted conditions arises from a warm-rain source limitation.

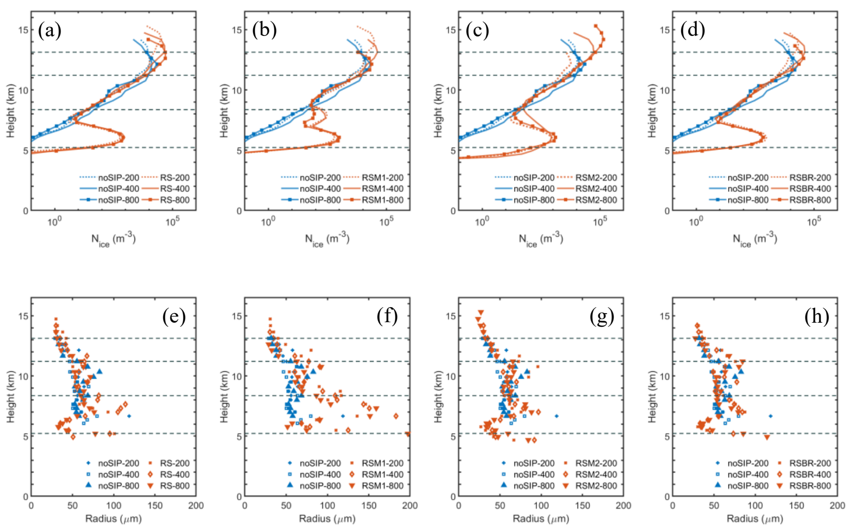

Figure 10. Vertical profiles of horizontally averaged (a-d) ice crystal number concentration (N_{ice}) and (e-h) ice crystal mean-mass radius from simulations without SIP (noSIP) and with different SIP configurations: (a, e) RS, (b, f) RSM1, (c, g) RSM2, and (d, h) RSBR. Dotted lines denote $N_d = 200$ cm^{-3}, solid lines denote $N_d = 400$ cm^{-3}, and solid lines with square markers denote $N_d = 800$ cm^{-3}. All profiles are averaged over regions with IWC > 0.01 g m^{-3} during 02:30–08:30 UTC on 6 February 2006. Gray dashed lines indicate the 0, −20, −40, and −60 °C isotherms. Equivalent plots for cloud droplet and rain properties are shown in Figures S3–S4 in the Supplement.

https://doi.org/10.5194/egusphere-2025-5665
Preprint. Discussion started: 19 November 2025

For RSM2, the ice crystal number concentration shows little sensitivity to CCN below ~7 km, whereas between 7 and 9 km it is highest at N_d = 400 cm^{-3}, lower at N_d = 800 cm^{-3}, and lowest at N_d = 200 cm^{-3} (Figure 10c). Unlike Mode 1 (RSM1), Mode 2 (RSM2) relies on collisions between raindrops and large ice particles, such as graupel. Therefore, we examine graupel characteristics to assess the efficiency of Mode 2 under different CCN levels. As shown in Figure 11, graupel number in 5–9 km exceeds noSIP and generally decreases with increasing CCN. The graupel radius is smallest at N_d = 200 cm^{-3} (~240 μm) and larger at 400–800 cm^{-3} (~400 μm) between 5 and 7 km, and this contrast remains at higher levels. Clean conditions (N_d = 200 cm^{-3}) also promote earlier warm rain, reducing supercooled liquid at upper levels and limiting liquid–ice overlap with sufficiently large graupel. Together, smaller graupel and reduced overlap lower the likelihood of effective collisions and suppress Mode 2 efficiency. In contrast, at N_d = 400 cm^{-3}, both liquid water and graupel size are more favorable, consistent with the ΔIWC maximum at N_d = 400 cm^{-3} and the minimum at N_d = 200 cm^{-3}. Overall, Mode 2 is suppressed under clean conditions due to smaller graupel, weaker liquid–ice overlap, and the reduced likelihood of effective collisions.

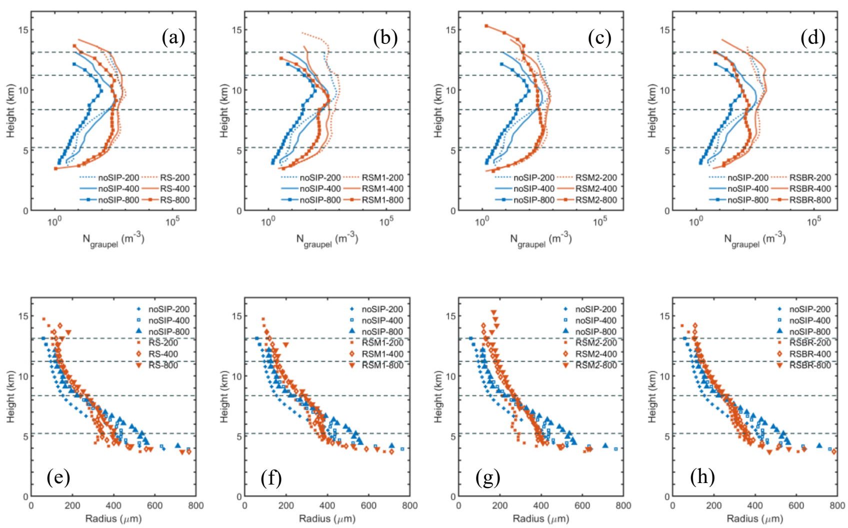

Figure 11. Same as Figure 10, but for (a-d) graupel number concentration ($N_{graupel}$), and (e-h) graupel mean-mass radius.

https://doi.org/10.5194/egusphere-2025-5665
Preprint. Discussion started: 19 November 2025

4 Discussion

4.1 SIP–CCN effects on radiation and precipitation

The experiments show that SIP alters the radiative and precipitation characteristics of the 6 February 2006 storm, but its impacts depend on CCN concentrations. Under moderate aerosol loading (N_d = 400 cm^{-3}), SIP produces the largest reduction in outgoing longwave radiation (OLR), expansion of low-OLR anvil areas, and the strongest enhancement of organized precipitation, in closer agreement with satellite and radar observations (Figures 2–6). By contrast, SIP effects are weaker under clean (N_d = 200 cm^{-3}) and polluted conditions (N_d = 800 cm^{-3}), and the OSR response is overall modest and varies in sign with CCN. These results highlight a nonlinear SIP–CCN influence on storm structure and radiative forcing.

The underlying mechanisms can be linked to the modulation of cloud microphysics by CCN. At low CCN, large droplets form and precipitation develops early through warm-rain processes, depleting supercooled liquid water and leaving little available for SIP-induced ice growth. As a result, OLR reduction and precipitation changes are limited. At high CCN, numerous small droplets delay warm-rain processes and sustain supercooled liquid water at higher altitudes. The reduced collision–coalescence efficiency leads to the lowest accumulated rainfall in noSIP-800 among the three CCN levels (Figure 6b). When SIP is activated, this additional supercooled liquid water provides a source for secondary ice production. The extra ice particles enhance riming and graupel formation, and subsequent melting increases surface rainfall, so allSIP-800 yields more rainfall than noSIP-800. However, the SIP-related increase remains smaller than at N_d = 400 cm^{-3}, because at moderate CCN the mixed-phase layer contains a more favorable combination of supercooled liquid water, raindrops, and large rimed particles within the temperature ranges where the SIP mechanisms are active, allowing more efficient ice growth and melt out. At moderate CCN, the SIP mechanisms therefore act together most effectively, leading to stronger upper-level ice growth, thicker and more organized anvils, a larger reduction in OLR (Figures 2, 4), and enhanced rainfall that agrees better with the observations (Figures 5, 6). Thus, SIP partly compensates for warm rain suppression under polluted conditions, but its strongest combined radiative and precipitation impact occurs at moderate CCN, where the microphysical environment most strongly supports secondary ice production and conversion to surface rainfall.

This non-linear response should also be interpreted in the context of the weak-CAPE environment of this case (CAPE ≈ 1010 J kg^{-1}; Figure 1b). With limited instability, the balance between warm-rain and ice-phase processes could be more sensitive to CCN perturbations. In contrast, our earlier pre-

https://doi.org/10.5194/egusphere-2025-5665
Preprint. Discussion started: 19 November 2025

monsoon case (Sun et al., 2025), characterized by higher CAPE and stronger convection, showed larger reductions in OLR, stronger increases in OSR, and suppressed precipitation in allSIP compared to noSIP. This enhanced radiative signal arose from deeper and more persistent anvils formed under high CAPE. Vigorous updrafts transported large amounts of hydrometeors into the upper troposphere, strengthening both longwave cooling and shortwave reflection (Feng et al., 2011; Hartmann and Berry, 2017). At the same time, stronger glaciation converted more supercooled liquid water into ice particles, enhancing the formation of precipitation particles in the upper levels. However, much of this ice was retained in anvils or sublimates/melts before reaching the ground, leading to reduced surface rainfall despite greater ice production (Han et al., 2024; Grzegorczyk et al., 2025a). By contrast, in the weak-CAPE 6 February 2006 storm, OLR responses remain robust but OSR is only weakly affected (Figures 2, 4). SIP enhances OSR at N_d = 400 cm^{-3}, but this effect reverses at N_d = 200 cm^{-3} and nearly vanishes at N_d = 800 cm^{-3}. This weak and non-monotonic OSR response likely reflects the combined influences of changes in anvil coverage, optical depth and particle size, and the timing of SIP-induced anvils relative to the maximum solar insolation. As a result, shortwave fluxes exhibit the SIP signal much less clearly than longwave cooling in this case. This behavior is consistent with Finney et al. (2025), who showed across 12 convective cases that changes in cloud droplet number, ice nucleating particles, and secondary ice configurations can modify anvil albedo and high cloud area, but that these shortwave responses are generally small compared with the case to case spread, highlighting the strong role of environmental variability and the need for caution when interpreting single case results. Meanwhile, precipitation increases in allSIP relative to noSIP (Figures 5, 6). Under weak instability, cloud depth and anvil extent are limited compared to the high-CAPE case. SIP generates additional ice particles that promote riming and subsequently melt as they fall, providing an extra source of surface rainfall. This explains why SIP increases precipitation in the 6 February 2006 case, in contrast to the suppression observed in the pre-monsoon case.

These results underscore the importance of considering environmental conditions, such as CAPE, when assessing SIP-CCN interactions in tropical convection. Across both radiation and precipitation responses, the strongest enhancement consistently occurs under moderate CCN, indicating that SIP plays an important role in amplifying aerosol effects on tropical convection, particularly under weakly unstable environments.

https://doi.org/10.5194/egusphere-2025-5665
Preprint. Discussion started: 19 November 2025

4.2 Sensitivity to SIP mechanisms and model uncertainties

The aerosol response of secondary ice production is mechanism dependent and non-linear. RSM1 is suppressed under polluted conditions (N_d = 800 cm^{-3}), RSM2 is inhibited under clean conditions (N_d = 200 cm^{-3}), and RS together with RSBR show limited CCN sensitivity. The combined effect produces the strongest signals at moderate CCN (N_d = 400 cm^{-3}), including enhanced upper-level ice, higher peak updrafts, and the largest reduction of outgoing longwave radiation (Figures 9–11; Table 3).

For RSM1, the diagnostics indicate a limitation in the warm-branch supply. Mode 1 depends on the freezing of supercooled raindrops and their collisions with small ice particles. Under high CCN, cloud droplets are more numerous and smaller, collision–coalescence proceeds more slowly, and the delivery of raindrops into the 0 to −20 °C layer is reduced. Consistently, RSM1 exhibits less ice number between 7 and 9 km and the smallest ΔIWC at N_d = 800 cm^{-3}, while crystal sizes remain nearly unchanged across CCN levels (Figure 10; Table 3).

For RSM2, Mode 2 depends on encounters between raindrops and large rimed ice particles. In clean conditions, warm rain forms and precipitation begins earlier, which limits the overlap of supercooled liquid and large ice in the 7–9 km layer. The diagnostics show the lowest upper-level ice number and the smallest graupel radii at N_d = 200 cm^{-3}, whereas moderate to high CCN maintains larger graupel and stronger upper-level ice production, with ΔIWC maximized at N_d = 400 cm^{-3} (Figure 11; Table 3).

Our simulations further demonstrate that the allSIP configuration produces the strongest enhancement at moderate CCN (N_d = 400 cm^{-3}). This non-linear behavior reflects the need for supercooled raindrops and sufficiently large rimed ice to co-exist within the mixed-phase layer (Phillips et al., 2018; Keinert et al., 2020; James et al., 2021). Under clean and polluted conditions, one of the droplet-shattering pathways is limited: Mode 1 at high CCN due to the reduced supply of supercooled raindrops, and Mode 2 at low CCN because collisions with large rimed ice particles are less frequent in the mixed-phase layer. At moderate CCN, supercooled liquid is available, and raindrops occur with larger rimed ice, allowing Mode 1 and Mode 2 to operate concurrently on top of the relatively CCN-insensitive RS and BR processes. As a result, the combined SIP contribution is largest at intermediate aerosol loading, yielding the greatest ΔIWC and clear dynamical and radiative responses (Figures 4, 6, 7). This peak at intermediate aerosol loading is consistent with previous observational and modeling studies (Rosenfeld et al., 2008; Fan et al., 2016), and our results identify SIP as a process pathway that helps produce this non-linear CCN dependence. This response likely arises because the amounts of supercooled liquid water

https://doi.org/10.5194/egusphere-2025-5665
Preprint. Discussion started: 19 November 2025

and rimed ice, which are controlled by N_d, do not change in a simple way across the temperature ranges where each SIP mechanism is most active. Different SIP parameterizations, with other temperature ranges or production rates, could change this relationship and in some cases produce a more monotonic response to N_d. However, the general result that aerosol control of liquid and ice in the mixed-phase layer affects the strength of SIP is expected to remain.

Beyond this CCN dependence, our results also indicate that droplet shattering mechanisms (Mode 1 and Mode 2) contribute more strongly to ice production than ice–ice collisional breakup (BR). This suggests that interactions between raindrops and ice particles can play an important role in sustaining secondary ice production under the simulated conditions. However, Grzegorczyk et al. (2025b) found that BR and RS were the most effective SIP mechanisms in reproducing ice numbers in deep convections, while droplet shattering played a minor role. Part of this difference may arise from the microphysical and environmental conditions in our simulations, where graupel sizes and collision energies are relatively modest (Sun et al., 2025), which limits the efficiency of BR. Another possible explanation is the treatment of raindrop freezing in two modeling systems. UM-CASIM employs a formulation based on Bigg (1953) with modified parameter values, which affects the number of freezing raindrops and graupel particles formed in the mixed phase region where droplet shattering can occur. By contrast, the bin microphysics model DESCAM uses the original Bigg (1953) scheme (Grzegorczyk et al., 2025b), which tends to produce fewer freezing raindrops (e.g., Morrison et al., 2005; Fan et al., 2009; Sullivan et al., 2018) and thus fewer opportunities for droplet shattering, so that BR and RS account for a larger share of the simulated secondary ice. Environmental differences, such as CAPE, liquid water content, may also contribute to the SIP responses. These results highlight the uncertainties in quantifying the relative importance of SIP mechanisms. Consistent parameterizations and further observational constraints are still needed to separate the contributions of raindrop shattering and collisional breakup in deep convective clouds.

5 Conclusions

This study examines how secondary ice production (SIP) interacts with aerosol loading to affect tropical convection, using the 6 February 2006 Darwin storm as a weak-CAPE case. The results show that SIP significantly alters cloud radiative properties, precipitation characteristics, and storm microphysics, with the strongest effects occurring at moderate aerosol concentrations ($N_d = 400\ cm^{-3}$).

https://doi.org/10.5194/egusphere-2025-5665
Preprint. Discussion started: 19 November 2025

Microphysically, SIP substantially enhances the ice phase. At $N_d = 400\ cm^{-3}$, ice crystal number concentration (N_{ice}) exceeds $3 \times 10^3\ m^{-3}$ at temperatures warmer than –10 °C, more than three orders of magnitude above noSIP. Ice crystals also grow larger, with mean-mass radii exceeding 100 μm, and ice water content (IWC) increases by up to 121.7%. Relative to the corresponding noSIP runs, graupel number concentration increases at all CCN levels, although the graupel radius decreases due to enhanced competition for liquid water. These changes strengthen latent heating and vertical motion, with the strongest updrafts ($W_{max} = 12.6\ m\ s^{-1}$) at $N_d = 400\ cm^{-3}$, compared with $10.5\ m\ s^{-1}$ at $N_d = 800\ cm^{-3}$ and $9.1\ m\ s^{-1}$ at $N_d = 200\ cm^{-3}$.

At the macroscale, SIP enhances both radiation and precipitation responses, but primarily under moderate aerosol loading. At $N_d = 400\ cm^{-3}$, SIP reduces outgoing longwave radiation (OLR) by 6.86 W m^{-2} (–2.5%) and expands the low-OLR cloud cover by ~25–30%, in better agreement with satellite observations. In contrast, the OLR response is weaker and spatially fragmented at $N_d = 800\ cm^{-3}$ (–3.34 W m^{-2}, –1.2%), and small and of opposite sign at $N_d = 200\ cm^{-3}$ (+0.61 W m^{-2}, +0.2%). Changes in outgoing shortwave radiation (OSR) are smaller and vary in sign, with a clear increase only at $N_d = 400\ cm^{-3}$ (+7.95 W m^{-2}).

SIP also reorganizes rainfall patterns. At $N_d = 400\ cm^{-3}$, rainfall becomes more organized, producing stronger and more concentrated precipitation patterns that closely match radar observations. The domain-averaged peak rainfall rate rises from 0.80 to 1.35 mm h^{-1}, and total accumulation increases by ~25%. At $N_d = 800\ cm^{-3}$, rainfall becomes more spatially fragmented, and at $N_d = 200\ cm^{-3}$ the impact is small or negative, with peak rainfall rate suppressed.

Sensitivity experiments show distinct CCN responses among SIP mechanisms. RSM1 (RS + Mode 1) is most active at moderate CCN (ΔIWC = +0.12 g m^{-3} at $N_d = 400\ cm^{-3}$) but weakens at high CCN (+0.03 g m^{-3} at $N_d = 800\ cm^{-3}$), owing to a reduced supply of supercooled raindrops in the mixed-phase layer. RSM2 (RS + Mode 2) is strongest at moderate CCN (ΔIWC = +0.17 g m^{-3} at $N_d = 400\ cm^{-3}$), but weakens at lower CCN (+0.03 g m^{-3} at $N_d = 200\ cm^{-3}$), where collisions with larger rimed ice particles are less frequent. RS and RSBR are relatively less sensitive to CCN. Their combined contribution peaks at intermediate CCN, producing the largest ΔIWC and clear dynamical and radiative responses.

Nevertheless, the CCN sensitivity of individual SIP mechanisms remains uncertain, due to differences in parameterizations, model frameworks, and environmental conditions. Constraining these responses through observations and targeted modeling will be essential for improving their representation across a range of aerosol regimes.

https://doi.org/10.5194/egusphere-2025-5665
Preprint. Discussion started: 19 November 2025

Tables

660 **Table 1. Model experiment overview.**

Cloud droplet number	Type of secondary ice production					
(cm^{-3})	all-SIP	no-SIP	RS	RS+M1	RS+M2	RS+BR
200	allSIP-200	noSIP-200	RS-200	RSM1-200	RSM2-200	RSBR-200
400	allSIP-400	noSIP-400	RS-400	RSM1-400	RSM2-400	RSBR-400
800	allSIP-800	noSIP-800	RS-800	RSM1-800	RSM2-800	RSBR-800

Note: RS refers to rime-splintering (Hallett and Mossop, 1974); M1 and M2 indicate two droplet shattering modes (Phillips et al., 2018); BR denotes ice-ice collisional breakup (Phillips et al., 2017).

Table 2. Comparison of radiation responses to SIP across CCN levels.

	N_d (cm^{-3})	Mean OLR (W m^{-2})	ΔOLR (W m^{-2})	Relative change	Mean OSR (W m^{-2})	ΔOSR (W m^{-2})	Relative change
allSIP	200	270.10	+0.61	+0.2%	363.63	-6.55	-1.8%
	400	263.36	-6.86	-2.5%	400.85	+7.95	+2.0%
	800	266.54	-3.34	-1.2%	420.38	-4.05	-0.9%
noSIP	200	269.49	—	—	370.18	—	—
	400	270.22	—	—	392.90	—	—
	800	269.88	—	—	424.43	—	—

665 Note: All values are calculated over the analysis region shown in Figure 1a, during 02:30–08:30 UTC on 6 February 2006. ΔOLR and ΔOSR represent the differences between SIP and noSIP simulations. Relative change (%) is calculated as $(OLR_{SIP} - OLR_{noSIP})/OLR_{noSIP} \times 100\%$, and similarly for OSR.

https://doi.org/10.5194/egusphere-2025-5665
Preprint. Discussion started: 19 November 2025

Table 3. Comparison of IWC and updraft responses to SIP mechanisms across CCN levels.

		IWC			Updrafts	
	N_d (cm^{-3})	ΔIWC ($g\ m^{-3}$)	Relative change	Peak altitude (km)	W_{max} ($m\ s^{-1}$)	Peak altitude (km)
RS	200	+0.17	+84.6%	7	10.0	5.5
	400	+0.13	+86.4%	10	11.3	6.1
	800	+0.08	+39.9%	6	11.3	6.1
RSM1	200	+0.10	+47.4%	10	11.0	4.9
	400	+0.12	+78.1%	10	10.2	6.4
	800	+0.03	+14.1%	6	9.5	6.1
RSM2	200	+0.03	+16.4%	7	10.2	5.2
	400	+0.17	+109.7%	10	11.2	5.5
	800	+0.08	+44.1%	10	12.2	6.7
RSBR	200	+0.09	+46.5%	7	9.8	5.8
	400	+0.16	+106.4%	10	11.9	6.4
	800	+0.06	+29.0%	6	11.3	4.4
all-SIP	200	+0.05	+26.8%	7	9.1	5.2
	400	+0.19	+121.7%	10	12.6	5.5
	800	+0.16	+87.9%	10	10.5	4.7

Note: ΔIWC is taken at the time of maximum difference between SIP and noSIP simulations. Relative change (%) is calculated as $(IWC_{SIP} - IWC_{noSIP})/IWC_{noSIP} \times 100\%$. Peak altitudes correspond to the vertical levels where ΔIWC or W_{max} reaches its maximum for each configuration.

675 *Data availability.* The simulation data in this study are archived on the UK Met Office MASS system (suite ID: u-dh136) and accessible via the JASMIN platform (http://www.jasmin.ac.uk/, last access: 14 Nov 2025). The CASIM microphysics code with the integrated SIP parameterizations is hosted on the Met Office Science Repository Service (MOSRS): https://code.metoffice.gov.uk/trac/monc/log/casim/branches/dev/mengyusun/r10208_SIP_rep (last access: 14 Nov 2025).

680 *Author contributions.* MS and PJC formulated the research objectives and designed the experiments. PRF provided advice on SIP mechanism analysis and supported the UM-CASIM configuration. MS performed the simulations and analysis with input from PRF, DLF, and AMB. MS prepared the manuscript with contributions from all co-authors.

Competing interests. The authors declare that they have no conflict of interest.

Acknowledgements. This study was funded by the Natural Environment Research Council (NERC) under the DCMEX project (Grant NE/T006420/1) and the Horizon Europe CERTAINTY project (Grant agreement No. 101137680). We acknowledge the Met Office and NERC for providing access to the Monsoon high-performance computing facility. Data storage and processing were supported by the UK Centre for Environmental Data Analysis (CEDA) via the JASMIN platform (https://doi.org/10.1109/BigData.2013.6691556).

https://doi.org/10.5194/egusphere-2025-5665
Preprint. Discussion started: 19 November 2025

References

Boutle, I. A., Eyre, J. E. J., and Lock, A. P.: Seamless stratocumulus simulation across the turbulent gray zone, Mon. Weather Rev., 142, 1655–1668, https://doi.org/10.1175/MWR-D-13-00229.1, 2014.

Bigg, E.K.: The formation of atmospheric ice crystals by the freezing of droplets, Q.J.R. Meteorol. Soc., 79, 510–519, https://doi.org/10.1002/qj.49707934207, 1953.

Bush, M., Flack, D. L. A., Lewis, H. W., Bohnenstengel, S. I., Short, C. J., Franklin, C., Lock, A. P., Best, M., Field, P., McCabe, A., Van Weverberg, K., Berthou, S., Boutle, I., Brooke, J. K., Cole, S., Cooper, S., Dow, G., Edwards, J., Finnenkoetter, A., Furtado, K., Halladay, K., Hanley, K., Hendry, M. A., Hill, A., Jayakumar, A., Jones, R. W., Lean, H., Lee, J. C. K., Malcolm, A., Mittermaier, M., Mohandas, S., Moore, S., Morcrette, C., North, R., Porson, A., Rennie, S., Roberts, N., Roux, B., Sanchez, C., Su, C.-H., Tucker, S., Vosper, S., Walters, D., Warner, J., Webster, S., Weeks, M., Wilkinson, J., Whitall, M., Williams, K. D., and Zhang, H.: The third Met Office Unified Model–JULES Regional Atmosphere and Land Configuration, RAL3, Geosci. Model Dev., 18, 3819–3855, https://doi.org/10.5194/gmd-18-3819-2025, 2025.

Bush, M., Boutle, I., Edwards, J., Finnenkoetter, A., Franklin, C., Hanley, K., Jayakumar, A., Lewis, H., Lock, A., Mittermaier, M., Mohandas, S., North, R., Porson, A., Roux, B., Webster, S., and Weeks, M.: The second Met Office Unified Model–JULES Regional Atmosphere and Land configuration, RAL2, Geosci. Model Dev., 16, 1713–1734, https://doi.org/10.5194/gmd-16-1713-2023, 2023.

Connolly, P. J., Vaughan, G., May, P. T., Chemel, C., Allen, G., Choularton, T. W., Gallagher, M. W., Bower, K. N., Crosier, J. and Dearden, C.: Can aerosols influence deep tropical convection? Aerosol indirect effects in the Hector island thunderstorm, Q. J. R. Meteorol. Soc., 139, 2190–2208, https://doi.org/10.1002/qj.2083, 2013.

Cooper, W. A.: Ice Initiation in Natural Clouds, Meteorological Monographs, 43, 29–32, https://doi.org/10.1175/0065-9401-21.43.29, 1986.

Dedekind, Z., Lauber, A., Ferrachat, S., and Lohmann, U.: Sensitivity of precipitation formation to secondary ice production in winter orographic mixed-phase clouds, Atmos. Chem. Phys., 21, 15115–15134, https://doi.org/10.5194/acp-21-15115-2021, 2021.

Dye, J. E. and Hobbs, P. V.: The influence of environmental parameters on the freezing and fragmentation of suspended water drops, J. Atmos. Sci., 25, 82–96, https://doi.org/10.1175/1520-0469(1968)025,0082:TIOEPO.2.0.CO;2, 1968.

https://doi.org/10.5194/egusphere-2025-5665
Preprint. Discussion started: 19 November 2025

Edwards, J. M., and Slingo, A.: Studies with a flexible new radiation code. I: Choosing a configuration for a large-scale model, Quart. J. Roy. Meteorol. Soc., 122, 689–719, https://doi.org/10.1002/qj.49712253107, 1996.

Fan, J., Wang, Y., Rosenfeld, D., and Liu, X.: Review of Aerosol–Cloud Interactions: Mechanisms, Significance, and Challenges, J. Atmos. Sci., 73, 4221–4252, https://doi.org/10.1175/JAS-D-16-0037.1, 2016.

Fan, J., Ovtchinnikov, M., Comstock, J. M., McFarlane, S. A., and Khain, A.: Ice formation in Arctic mixed-phase clouds: Insights from a 3-D cloud-resolving model with size-resolved aerosol and cloud microphysics, J. Geophys. Res., 114, D04205, https://doi.org/10.1029/2008JD010782, 2009.

Feng, Z., Dong, X., Xi, B., Schumacher, C., Minnis, P., and Khaiyer, M.: Top-of-atmosphere radiation budget of convective core/stratiform rain and anvil clouds from deep convective systems, J. Geophys. Res., 116, D23202, https://doi.org/10.1029/2011JD016451, 2011.

Field, P. R., Hill, A., Shipway, B., Furtado, K., Wilkinson, J., Miltenberger, A., Gordon, H., Grosvenor D. P., Stevens, R., and Van Weverberg, K.et al.: Implementation of a double moment cloud microphysics scheme in the UK met office regional numerical weather prediction model, Q. J. Roy. Meteorol. Soc., 149, 703–739, https://doi.org/10.1002/qj.4414, 2023.

Field, P. R., Lawson, R. P., Brown, P. R. A., Lloyd, G., Westbrook, C., Moisseev, D., Miltenberger, A., Nenes, A., Blyth, A., Choularton, T., Connolly, P., Buehl, J., Crosier, J., Cui, Z., Dearden, C., DeMott, P., Flossmann, A., Heymsfield, A., Huang, Y., Kalesse, H., Kanji, Z. A., Korolev, A., Kirchgaessner, A., Lasher-Trapp, S., Leisner, T., McFarquhar, G., Phillips, V., Stith, J., and Sullivan, S.: Chapter 7. Secondary Ice Production- current state of the science and recommendations for the future, Meteorological Monographs, https://doi.org/10.1175/amsmonographs-d-16-0014.1, 2017.

Finney, D. L., Blyth, A. M., Field, P. R., Daily, M. I., Murray, B. J., Sun, M., Connolly, P. J., Cui, Z., and Böing, S.: Microphysical fingerprints in anvil cloud albedo, Atmos. Chem. Phys., 25, 10907–10929, https://doi.org/10.5194/acp-25-10907-2025, 2025.

Grabowski, W. W. and Morrison, H.: Do Ultrafine Cloud Condensation Nuclei Invigorate Deep Convection?, J. Atmos. Sci., 77, 2567–2583, https://doi.org/10.1175/JAS-D-20-0012.1, 2020.

Grzegorczyk, P., Yadav, S., Zanger, F., Theis, A., Mitra, S. K., Borrmann, S., and Szakáll, M.: Fragmentation of ice particles: laboratory experiments on graupel–graupel and graupel–snowflake collisions, Atmos. Chem. Phys., 23, 13505–13521, https://doi.org/10.5194/acp-23-13505-2023, 2023.

https://doi.org/10.5194/egusphere-2025-5665
Preprint. Discussion started: 19 November 2025

Grzegorczyk, P., Wobrock, W., Canzi, A., Niquet, L., Tridon, F., and Planche, C.: Investigating secondary ice production in a deep convective cloud with a 3D bin microphysics model: Part II- Effects on the cloud formation and development, Atmospheric Research, 314, 107797, https://doi.org/10.1016/j.atmosres.2024.107797, 2025a.

Grzegorczyk, P., Wobrock, W., Canzi, A., Niquet, L., Tridon, F., and Planche, C.: Investigating secondary ice production in a deep convective cloud with a 3D bin microphysics model: Part I- Sensitivity study of microphysical processes representations, Atmospheric Research, 313, 107774, https://doi.org/10.1016/j.atmosres.2024.107774, 2025b.

Hallett, J. and Mossop, S. C.: Production of secondary ice particles during the riming process, Nature, 249, 26–28, https://doi.org/10.1038/249026a0, 1974.

Han, C., Hoose, C., and Dürlich, V.: Secondary Ice Production in Simulated Deep Convective Clouds: A Sensitivity Study, J. Atmos. Sci., 81, 903–921, https://doi.org/10.1175/jas-d-23-0156.1, 2024.

Hartmann, D. L., and Berry, S. E.: The balanced radiative effect of tropical anvil clouds, J. Geophys. Res. Atmos., 122, 5003–5020, https://doi.org/10.1002/2017JD026460, 2017.

Hawker, R. E., Miltenberger, A. K., Wilkinson, J. M., Hill, A. A., Shipway, B. J., Cui, Z., Cotton, R. J., Carslaw, K. S., Field, P. R., and Murray, B. J.: The temperature dependence of ice-nucleating particle concentrations affects the radiative properties of tropical convective cloud systems, Atmos. Chem. Phys., 21, 5439–5461, https://doi.org/10.5194/acp-21-5439-2021, 2021a.

Hawker, R. E., Miltenberger, A. K., Johnson, J. S., Wilkinson, J. M., Hill, A. A., Shipway, B. J., Field, P. R., Murray, B. J., and Carslaw, K. S.: Model emulation to understand the joint effects of ice-nucleating particles and secondary ice production on deep convective anvil cirrus, Atmos. Chem. Phys., 21, 17315–17343, https://doi.org/10.5194/acp-21-17315-2021, 2021b.

Hobbs, P. V., and Rangno, A. L.: Ice Particle Concentrations in Clouds, J. Atmos. Sci., 42, 2523–2549, https://doi.org/10.1175/1520-0469(1985)042<2523:IPCIC>2.0.CO;2, 1985.

Huang, Y., Wu, W., McFarquhar, G. M., Xue, M., Morrison, H., Milbrandt, J., Korolev, A. V., Hu, Y., Qu, Z., Wolde, M., Nguyen, C., Schwarzenboeck, A., and Heckman, I.: Microphysical processes producing high ice water contents (HIWCs) in tropical convective clouds during the HAIC-HIWC field campaign: dominant role of secondary ice production, Atmos. Chem. Phys., 22, 2365–2384, https://doi.org/10.5194/acp-22-2365-2022, 2022.

Huang, S., Yang, J., Li, J., Chen, Q., Zhang, Q., and Guo, F.: Impact of secondary ice production on thunderstorm electrification under different aerosol conditions, Atmos. Chem. Phys., 25, 1831–1850,

https://doi.org/10.5194/egusphere-2025-5665
Preprint. Discussion started: 19 November 2025

https://doi.org/10.5194/acp-25-1831-2025, 2025.

Jackson, R., Collis, S., Louf, V., Protat, A., Wang, D., Giangrande, S., Thompson, E. J., Dolan, B., and Powell, S. W.: The development of rainfall retrievals from radar at Darwin, Atmos. Meas. Tech., 14, 53–69, https://doi.org/10.5194/amt-14-53-2021, 2021.

James, R. L., Phillips, V. T. J., and Connolly, P. J.: Secondary ice production during the break-up of freezing water drops on impact with ice particles, Atmos. Chem. Phys., 21, 18519–18530, https://doi.org/10.5194/acp-21-18519-2021, 2021.

James, R. L., Crosier, J., and Connolly, P. J.: A bin microphysics parcel model investigation of secondary ice formation in an idealised shallow convective cloud, Atmos. Chem. Phys., 23, 9099–9121, https://doi.org/10.5194/acp-23-9099-2023, 2023.

Jeffery, C. A. and Austin, P. H.: Homogeneous nucleation of supercooled water: Results from a new equation of state, J. Geophys. Res., 102, 25269–25279, https://doi.org/10.1029/97JD02243, 1997.

Keinert, A., Spannagel, D., Leisner, T., and Kiselev, A.: Secondary ice production upon freezing of freely falling drizzle droplets, J. Atmos. Sci., 77, 2959–2967, https://doi.org/10.1175/JAS-D-20 0081.1, 2020.

Khain, A., Rosenfeld, D., and Pokrovsky, A.: Aerosol impact on the dynamics and microphysics of deep convective clouds, Q. J. Roy. Meteor. Soc., 131, 2639–2663, https://doi.org/10.1256/qj.04.62, 2005.

Korolev, A. and Leisner, T.: Review of experimental studies of secondary ice production, Atmos. Chem. Phys., 20, 11767–11797, https://doi.org/10.5194/acp-20-11767-2020, 2020.

Ladino, L. A., Korolev, A., Heckman, I., Wolde, M., Fridlind, A. M., and Ackerman, A. S.: On the role of ice-nucleating aerosol in the formation of ice particles in tropical mesoscale convective systems, Geophys. Res. Lett., 44, 1574–1582, https://doi.org/10.1002/2016GL072455, 2017.

Lauber, A., Kiselev, A., Pander, T., Handmann, P., and Leisner, T.: Secondary Ice Formation during Freezing of Levitated Droplets, J. Atmos. Sci., 75, 2815–2826, https://doi.org/10.1175/jas-d-18-0052.1, 2018.

Lock, A. P., Brown, A. R., Bush, M. R., Martin, G. M., and Smith, R. N. B.: A New Boundary Layer Mixing Scheme. Part I: Scheme Description and Single-Column Model Tests, Mon. Wea. Rev., 128, 3187-3199, https://doi.org/10.1175/1520-0493(2000)128<3187:ANBLMS>2.0.CO;2, 2000.

Louf, V., Protat, A., Warren, R. A., Collis, S. M., Wolff, D. B., Raunyiar, S., Jakob, C., and Petersen, W. A.: An Integrated Approach to Weather Radar Calibration and Monitoring Using Ground Clutter and

Satellite Comparisons, J. Atmos. Ocean. Technol., 36, 17–39, https://doi.org/10.1175/JTECH-D-18-0007.1, 2019.

Manners, J., Edwards, J. M., Hill, P., and Thelen, J.-C.: SOCRATES (Suite Of Community RAdiative Transfer codes based on Edwards and Slingo) Technical Guide, Met Office, UK, https://code.metoffice.gov.uk/trac/socrates, last access: 14 Nov 2025.

May, P. T., Mather, J. H., Vaughan, G., Jakob, C., McFarquhar, G. M., Bower, K. N., and Mace, G. G.: The Tropical Warm Pool International Cloud Experiment. Bull. Amer. Meteor. Soc., 89, 629–646, https://doi.org/10.1175/BAMS-89-5-629, 2008.

Miltenberger, A. K., Field, P. R., Hill, A. H., and Heymsfield, A. J.: Vertical redistribution of moisture and aerosol in orographic mixed-phase clouds, Atmos. Chem. Phys., 20, 7979–8001, https://doi.org/10.5194/acp-20-7979-2020, 2020.

Morrison, H., Shupe, M. D., Pinto, J. O., and Curry, J. A.: Possible roles of ice nucleation mode and ice nuclei depletion in the extended lifetime of Arctic mixed-phase clouds, Geophys. Res. Lett., 32, L18801, https://doi.org/10.1029/2005GL023614, 2005.

Mossop, S. C.: Secondary ice particle production during rime growth: The effect of drop size distribution and rimer velocity, Q. J. Roy. Meteor. Soc., 111, 1113–1124, https://doi.org/10.1002/qj.49711147012, 1985.

NASA: Shuttle Radar Topography Mission (SRTM) Global, distributed by OpenTopography, https://doi.org/10.5069/G9445JDF, 2013.

Oraltay, R. G. and Hallett, J.: Evaporation and melting of ice crystals: A laboratory study, Atmos. Res., 24, 169–189, https://doi.org/10.1016/0169-8095(89)90044-6, 1989.

Phillips, V. T., Patade, S., Gutierrez, J., and Bansemer, A.: Secondary Ice Production by Fragmentation of Freezing Drops: Formulation and Theory, J. Atmos. Sci., 76, 3031–3070, https://doi.org/10.1175/JAS-D-17-0190.1, 2018.

Phillips, V. T. J., Yano, J.-I., and Khain, A.: Ice Multiplication by Breakup in Ice–Ice Collisions. Part I: Theoretical Formulation, J. Atmos. Sci., 74, 1705–1719, https://doi.org/10.1175/JAS-D-16-0224.1, 2017.

Qu, Y., Khain, A., Phillips, V., Ilotoviz, E., Shpund, J., Patade, S., and Chen, B.: The role of ice splintering on microphysics of deep convective clouds forming under different aerosol conditions: Simulations using the model with spectral bin microphysics, J. Geophys. Res., 125, e2019JD031312, https://doi.org/10.1029/2019JD031312, 2020.

Qu, Z., Korolev, A., Milbrandt, J. A., Heckman, I., Huang, Y., McFarquhar, G. M., Morrison, H., Wolde, M., and Nguyen, C.: The impacts of secondary ice production on microphysics and dynamics in tropical convection, Atmos. Chem. Phys., 22, 12287–12310, https://doi.org/10.5194/acp-22-12287-2022, 2022.

Rosenfeld, D., Lohmann, U., Raga, G. B., O'Dowd, C. D., Kulmala, M., Fuzzi, S., Reissell, A., and Andreae, M. O.: Flood or Drought: How Do Aerosols Affect Precipitation?, Science, 321, 1309–1313, https://doi.org/10.1126/science.1160606, 2008.

Rosenfeld, D. and Woodley, W. L.: Deep convective clouds with sustained supercooled liquid water down to −37.5 °C, Nature, 405, 440–442, https://doi.org/10.1038/35013030, 2000.

Sotiropoulou, G., Sullivan, S., Savre, J., Lloyd, G., Lachlan-Cope, T., Ekman, A. M. L., and Nenes, A.: The impact of secondary ice production on Arctic stratocumulus, Atmos. Chem. Phys., 20, 1301–1316, https://doi.org/10.5194/acp-20-1301-2020, 2020.

Sullivan, S. C., Barthlott, C., Crosier, J., Zhukov, I., Nenes, A., and Hoose, C.: The effect of secondary ice production parameterization on the simulation of a cold frontal rainband, Atmos. Chem. Phys., 18, 16461–16480, https://doi.org/10.5194/acp-18-16461-2018, 2018.

Sun, M., Liu, D., Qie, X., Mansell, E. R., Yair, Y., Fierro, A. O., Yuan, S., Chen, Z., and Wang, D.: Aerosol effects on electrification and lightning discharges in a multicell thunderstorm simulated by the WRF-ELEC model, Atmos. Chem. Phys., 21, 14141–14158, https://doi.org/10.5194/acp-21-14141-2021, 2021.

Sun, M., Li, Z., Wang, T., Mansell, E. R., Qie, X., Shan, S., et al.: Understanding the effects of aerosols on electrification and lightning polarity in an idealized supercell thunderstorm via model emulation, J. Geophys. Res. Atmos., 129, e2023JD039251, https://doi.org/10.1029/2023JD039251, 2024.

Sun, M., Connolly, P. J., Field, P. R., Finney, D. L., and Blyth, A. M.: Influence of secondary ice formation on tropical deep convective clouds simulated by the Unified Model, EGUsphere [preprint], https://doi.org/10.5194/egusphere-2025-3158, 2025.

Van Weverberg, K., Morcrette, C. J., Boutle, I., Furtado, K., and Field, P. R.: A Bimodal Diagnostic Cloud Fraction Parameterization. Part I: Motivating Analysis and Scheme Description, Mon. Wea. Rev., 149, 841-857, https://doi.org/10.1175/MWR-D-20-0224.1, 2021.

Varble, A. C., Igel, A. L., Morrison, H., Grabowski, W. W., and Lebo, Z. J.: Opinion: A critical evaluation of the evidence for aerosol invigoration of deep convection, Atmos. Chem. Phys., 23, 13791–13808, https://doi.org/10.5194/acp-23-13791-2023, 2023.

https://doi.org/10.5194/egusphere-2025-5665
Preprint. Discussion started: 19 November 2025

Vardiman, L.: The Generation of Secondary Ice Particles in Clouds by Crystal–Crystal Collision, J. Atmos. Sci., 35, 2168–2180, https://doi.org/10.1175/1520-0469(1978)035<2168:TGOSIP>2.0.CO;2, 1978.

Vaughan, G., Schiller, C., MacKenzie, A. R., Bower, K., Peter, T., Schlager, H., Harris, N. R. P., May, P. T.: SCOUT-O3/ACTIVE high-altitude aircraft measurements around deep tropical convection, Bull. Amer. Meteorol. Soc., 89, 647–662, https://doi.org/10.1175/BAMS-89-5-647, 2008.

Waman, D., Patade, S., Jadav, A., Deshmukh, A., Gupta, A. K., Phillips, V. T. J., Bansemer, A., and DeMott, P. J.: Dependencies of Four Mechanisms of Secondary Ice Production on Cloud-Top Temperature in a Continental Convective Storm, J. Atmos. Sci., 79, 3375–3404, https://doi.org/10.1175/JAS-D-21-0278.1, 2022.

Wood, N., Staniforth, A., White, A., Allen, T., Diamantakis, M., Gross, M., Melvin, T., Smith, C., Vosper, S., Zerroukat, M., and Thuburn, J.: An inherently mass-conserving semi-implicit semi-Lagrangian discretization of the deep-atmosphere global non-hydrostatic equations, Q. J. R. Meteorol. Soc., 140, 1505–1520, https://doi.org/10.1002/qj.2235, 2014.

Yin, J., and Porporato, A.: Diurnal cloud cycle biases in climate models, Nature Communications, 8, 2269, https://doi.org/10.1038/s41467-017-02369-4, 2017.

Young, G., Lachlan-Cope, T., O'Shea, S. J., Dearden, C., Listowski, C., Bower, K. N., Choularton, T. W., and Gallagher, M. W.: Radiative Effects of Secondary Ice Enhancement in Coastal Antarctic Clouds, Geophys. Res. Lett., 46, 2312–2321, https://doi.org/10.1029/2018gl080551, 2019.

Zhao, X., Liu, X., Phillips, V. T. J., and Patade, S.: Impacts of secondary ice production on Arctic mixed-phase clouds based on ARM observations and CAM6 single-column model simulations, Atmos. Chem. Phys., 21, 5685–5703, https://doi.org/10.5194/acp-21-5685-2021, 2021.